Full- f gyrokinetic simulations of Ohmic L-mode plasmas in linear and saturated Ohmic confinement regimes

Y. Idomura, G. Dif-Pradalier, X. Garbet, Y. Sarazin

full-f gyrokinetic simulations of ohmic L-mode plasmas in linear and saturated ohmic confinement regimes

Y. Idomura,[1] G. Dif-Pradalier,[2] X. Garbet,[2] Y. Sarazin,[2] and the Tore Supra Team[2, a)]
[1)] *JAEA, CCSE, Kashiwa, Chiba 277-0871, Japan*
[2)] *CEA, IRFM, F-13108 St. Paul-lez-Durance cedex, France*

(*Electronic mail: idomura.yasuhiro@jaea.go.jp)

(Dated: 7 March 2023)

Two time slices in linear and saturated ohmic confinement (LOC and SOC) regimes in a Tore Supra ohmic L-mode discharge are analyzed using nonlinear global full-f gyrokinetic simulations, and qualitative features of the LOC-SOC transition are reproduced. The exhaust of carbon impurity ions is caused by ion mixing, which is driven by the toroidal field stress. The intrinsic rotation develops in the opposite direction between the LOC and SOC phases, which is characterized by the different features of the mode asymmetry between trapped electron modes (TEMs) in the LOC phase and ion temperature gradient driven modes in the SOC phase, leading to the change of the profile shear stress. Here, the mode asymmetry or the ballooning angle depends not only on the profile shear and the E_r shear but also on the radial electric field E_r itself. The energy fluxes of electrons and deuterium ions are dominant in the LOC and SOC phases, respectively, and the ratio of the energy confinement time between two phases agree with the experimental value. Turbulent frequency spectra are characterized by quasi-coherent modes (QCMs) and broad-band spectra in the LOC and SOC phases, respectively. The QCMs are produced by a split of the toroidal mode number spectra of TEMs induced by the Doppler shift of poloidal $E \times B$ rotation due to E_r, which is sustained in the electron diamagnetic direction by the ripple induced counter-current rotation, and enhanced by higher temperature in the LOC phase.

I. INTRODUCTION

Ohmic L-mode discharges universally show a transition of the global energy confinement from the linear Ohmic confinement (LOC) regime, where the energy confinement time τ_E increases linearly with a density ramp, to the saturated Ohmic confinement (SOC) regime, where τ_E is saturated beyond certain critical density. This phenomenon is called as the LOC-SOC transition, and has been one of the long-standing issues in turbulent transport in magnetic confinement fusion devices[1,2]. The LOC-SOC transition is important not only for the energy confinement but also for particle and momentum transport. During the LOC-SOC transition, the exhaust of impurity ions was observed in several devices[3,4], and the reversal or change of intrinsic rotation was universally observed in many devices[2]. Since the control of impurity ions and intrinsic rotation is one of the critical issues in ITER, understanding of the LOC-SOC transition is important. The LOC-SOC transition is an interesting phenomenon also from the viewpoint of transport physics. Detailed turbulence measurements revealed the change of turbulent spectra, which are characterized by the so-called quasi-coherent modes (QCMs) and broad-band spectra in the LOC and SOC regimes, respectively[5–7]. Modulation experiments with edge cold pulses showed nonlocal transport in the LOC regime, while this feature disappeared in the SOC regime[4].

The LOC-SOC transition has been analyzed based on theory of micro-instabilities[3,8], linear gyrokinetic calculations[6,9–18], nonlinear gyrokinetic simulations[19–26], and transport models[21,22,27]. Many of these theoretical analyses showed transition of linearly most unstable modes from trapped electron modes (TEMs) to ion temperature gradient driven modes (ITGs), while the importance of a mixed mode state including subdominant modes was pointed out in Ref.18. Here, the density ramp increases a collisional stabilization effect of TEMs, while the exhaust of impurity ions reduces a dilution stabilization effect of ITGs. Gyrokinetic simulations of ITGs and TEMs were validated against fluctuation measurements. In Ref.21, the LOC-SOC transition on Alcator C-Mod was analyzed using nonlinear global δf gyrokinetic simulations, and turbulent spectra obtained from the phase contrast imaging in the experiment and from its synthetic diagnostics in the simulation showed qualitative agreements. In Refs.23 and 28, the LOC-SOC transition on Tore Supra was analyzed using nonlinear local δf gyrokinetic simulations, and turbulent spectra obtained from the reflectometry measurement in the experiment and its synthetic diagnostics in the simulation showed QCMs and broad-band spectra in the LOC and SOC regimes, respectively. Regarding turbulent transport, many works analyzed heat transport, while understanding of particle and momentum transport has not been matured. On Tore Supra, carbon impurity content in the LOC regime is at a non-tracer level, and the mechanism of the exhaust of carbon impurity ions, which is linked with transport of electrons and deuterium ions through the ambipolar condition, is still an open issue. A study on momentum transport leading to the change of intrinsic rotation is very limited, because non-diffusive momentum transport is induced by various symmetry breaking effects, which are not determined within local gyrokinetic models. The Coriolis pinch effect and the residual stress effect, in which the profile shear was prescribed, were examined against the ASDEX Upgrade (AUG) experiment using local gyrokinetic calculations, and the residual stress due to the shear of radial electric field E_r, which is determined by neoclassical poloidal rotation, and the profile shear was shown to be important[20]. On the other hand, in Ref. 24–26,

[a)] Y. Peysson and Tore Supra Team, Nuclear Fusion 41, 1703 (2001).

intrinsic rotation profiles in the DIII-D experiment were reproduced based on the balance between the diffusive momentum flux and the residual stress computed using nonlinear global δf gyrokinetic simulations with zero rotation. Here, the momentum diffusivity is estimated using the heat diffusivity and a given Prandtl number, and the turbulent residual stress was correlated with the shear of turbulent zonal flows and the turbulent intensity gradient. In Ref. 29, intrinsic rotation profiles in the AUG experiment were analyzed using nonlinear global δf gyrokinetic simulations, where rotation and density profiles are evolved, and it was shown that intrinsic flow gradients at experimental levels were formed mainly by the profile shear stress. Therefore, theoretical understanding of momentum transport is not converged, and further global simulations are needed. Finally, in spite of the development of gyrokinetic modeling and theory, any single model cannot capture all aspects of the above complicated physics in the LOC-SOC transition in a self-consistent manner.

To address this challenging issue, we need global full-f gyrokinetic models, which compute both plasma turbulence and plasma profiles in a self-consistent manner including multiple transport channels induced by collisional and turbulent transport. This capability enables us to study the following effects, which are important for understanding transport physics in the LOC-SOC transition. Firstly, the formation of intrinsic rotation is directly computed under the strict toroidal angular momentum conservation[30–32], in which in addition to the turbulent Reynolds stress, other mechanisms such as the neoclassical Reynolds stress, the toroidal field stress, and the $J \times B$ torque make significant contributions. Also, various symmetry breaking mechanisms such as the shear of the radial electric field E_r and zonal flows, the profile shear, and the turbulent intensity gradient are involved consistently, and their relative importance can be examined. Secondly, E_r is determined self-consistently, and the resulting effects such as the Doppler shift of turbulent spectra, turbulence suppression by the E_r shear, and the residual stress induced by E_r and E_r shear are analyzed in a straightforward manner. Thirdly, self-consistent interaction of multiple transport channels gives the following effects. The collisional ion-electron coupling determine the ion heating condition in Ohmic L-mode plasmas. Particle fluxes of electrons and multi-species ions satisfy the ambipolar condition, which is important in analyzing impurity transport at a non-tracer level. Particle and momentum transport channels are coupled through the toroidal angular momentum conservation. It is noted that in general, global δf gyrokinetic models or gradient driven simulations involve artificial source/sink terms everywhere in a plasma to fix plasma profiles, and neoclassical physics is excluded. Therefore, important conservation properties such as the toroidal angular momentum conservation and the ambipolar condition are not guaranteed or at least modified, which make study of the above effects difficult. In addition, former works on comparisons of flux driven global full-f gyrokinetic simulations and gradient driven global δf gyrokinetic simulations showed significantly different properties in avalanche like nonlocal transport, zonal flows, and staircase structures[33,34]. These motivate us to address the LOC-SOC transition via flux driven global full-f gyrokinetic simulations.

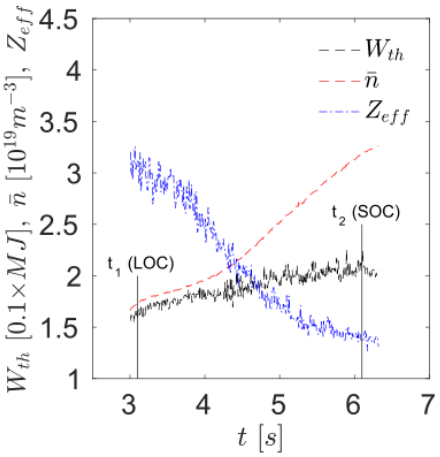

FIG. 1. Evolution of stored thermal energy W_{th}, line averaged density $\bar{n}$, and effective charge number Z_{eff} in Tore Supra ohmic L-mode discharge 48102. $t_1 \sim 3.1$s is in a LOC phase, and $t_2 \sim 6.1$s is in a SOC phase. Reproduced with permission from Plasma Phys. Control. Fusion 59, 064010 (2017)[23] . Copyright 2017 IOP Publishing.

In this study, we address the LOC-SOC transition on Tore Supra using the Gyrokinetic Toroidal 5D full-f Eulerian code GT5D[35–37], which computes an electrostatic global full-f model in multi-species plasmas with kinetic electrons. The conditions of numerical experiments are based on Tore Supra ohmic L-mode discharge 48102, which were already analyzed in detail based on nonlinear local δf gyrokinetic simulations[23]. The latter work showed validation studies on heat transport and turbulent spectra, while momentum transport and impurity transport have not been analyzed yet. In this work, we address all transport channels and the corresponding turbulent spectra with a single global full-f gyrokinetic model in a self-consistent manner.

The remainder of the paper is organized as follows. In Sec.II, the experimental data, calculation models, and simulation parameters are explained. In Sec.III, the validity of simulation parameters with scaled plasma sizes is discussed. In Sec.IV, numerical experiments in the LOC and SOC phases are presented, in which transport properties of particle, momentum, and energy transport are discussed, and turbulent spectra are analyzed. Finally, a summary is given in Sec.V.

II. CALCULATION MODEL

In this work, we analyze Tore Supra ohmic L-mode discharge 48102, which was discussed in detail in Refs.6, 14, 23, and 28. As shown in Figs.1 and 2, the discharge is characterized by a density ramp, leading to transition from the LOC regime to the SOC regime. In the LOC-SOC transition, the trend of the energy confinement time is changed from the linear increase proportional to the electron density to the saturation, the effective charge number Z_{eff} is decreased by ex-

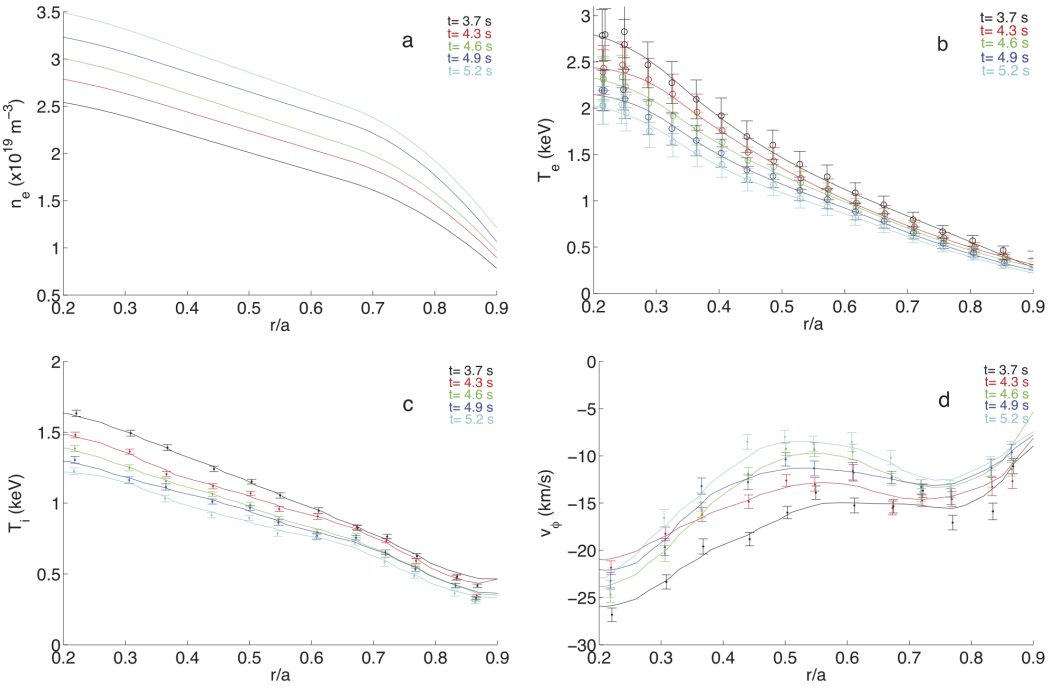

FIG. 2. (a) electron density, (b) electron temperature, (c) ion temperature, and (d) toroidal rotation profiles of carbon impurity ions at five time slices in Tore Supra ohmic L-mode discharge 48102. Reproduced with permission from Plasma Phys. Control. Fusion 57, 035002 (2015)[14]. Copyright 2015 IOP Publishing.

hausting carbon impurity ions, and the relative intrinsic rotation direction with respect to the edge rotation velocity is reversed (see Fig.2(d)). We focus on two time slices in the LOC and SOC regimes, $t_1 \sim 3.1$s and $t_2 \sim 6.1$s, which were analyzed in Ref.23. In the latter work, it was shown that the LOC and SOC phases are respectively dominated by TEM and ITG, and the electron temperature gradient driven mode is unstable only in the SOC phase.

Numerical experiments are conducted using GT5D, which computes electrostatic ion scale turbulence driven by ITG and TEM. In the gyro-center coordinates, $\mathbf{Z} = (t; \mathbf{R}, v_\parallel, \mu, \alpha)$, a conservative form of the electrostatic gyrokinetic equation is commonly used for all particle species including electron,

$$\frac{\partial \mathcal{J}_s f_s}{\partial t} + \nabla \cdot (\mathcal{J}_s \dot{\mathbf{R}} f_s) + \frac{\partial}{\partial v_\parallel}(\mathcal{J}_s \dot{v}_\parallel f_s) = \mathcal{J}_s \sum_{s'} C(f_s, f_{s'}) + \mathcal{J}_s S_{src,s} + \mathcal{J}_s S_{snk,s}, \quad (1)$$

$$\dot{\mathbf{R}} = v_\parallel \mathbf{b} + \mathbf{v}_E + \mathbf{v}_D, \quad (2)$$

$$\mathbf{v}_E = \frac{c}{q_s B_\parallel^*} \mathbf{b} \times (q_s \nabla \langle \phi \rangle_\alpha), \quad (3)$$

$$\mathbf{v}_D = \frac{c}{q_s B_\parallel^*} \mathbf{b} \times \left(m_s v_\parallel^2 \mathbf{b} \cdot \nabla \mathbf{b} + \mu \nabla B \right), \quad (4)$$

$$\dot{v}_\parallel = -\frac{\mathbf{B}^*}{m_s B_\parallel^*} \cdot (q_s \nabla \langle \phi \rangle_\alpha + \mu \nabla B) \quad (5)$$

where f_s denotes the guiding-center distribution function, $\mathcal{J}_s = m_s^2 B_\parallel^*$ is the Jacobian of the gyro-center coordinates, $C(f_s, f_{s'})$ is a multi-species Coulomb collision operator[38], $S_{src,s}$ and $S_{snk,s}$ are respectively the source and sink terms, $\mathbf{R}$ is the position of the guiding center, $\mathbf{v}$ is the velocity of the guiding center, $v_\parallel = \mathbf{b} \cdot \mathbf{v}$ and $v_\perp = |\mathbf{b} \times \mathbf{v}|$ are respectively the velocities in the parallel and perpendicular directions to the magnetic field, $\mu = m_s v_\perp^2 / 2B$ is the magnetic moment, α is the gyro-phase angle, $\mathbf{B} = B\mathbf{b}$ is the magnetic field, $\mathbf{b}$ is the unit vector in the parallel direction, m_s and q_s are respectively the mass and charge of the particle species s, c is the velocity of light, $\Omega_s = q_s B / m_s c$ is the cyclotron frequency, $B_\parallel^* = \mathbf{b} \cdot \mathbf{B}^*$ is a parallel component of $\mathbf{B}^* = \mathbf{B} + (B v_\parallel / \Omega_s) \nabla \times \mathbf{b}$, ϕ is the electrostatic potential of turbulent fields, and the gyro-averaging operator is defined as $\langle \cdot \rangle_\alpha \equiv \oint \cdot d\alpha / 2\pi$.

The electrostatic potential is determined using the hybrid kinetic electron model[37], where the gyrokinetic Poisson equation is modified as

$$-\sum_s \nabla_\perp \cdot \frac{\rho_{ts}^2}{\lambda_{Ds}^2} \nabla_\perp \phi_{n\neq 0} + \frac{\alpha_p}{\lambda_{De}^2} \phi_{n\neq 0} = 4\pi \left[\sum_{s\neq e} q_s \int f_{s,n\neq 0} \delta([\mathbf{R}+\rho] - \mathbf{x}) d^6 Z + q_e \int f_{e,t,n\neq 0} \delta([\mathbf{R}+\rho] - \mathbf{x}) d^6 Z \right], \quad (6)$$

$$-\sum_s \nabla_\perp \cdot \frac{\rho_{ts}^2}{\lambda_{Ds}^2} \nabla_\perp \phi_{n=0} = 4\pi \sum_s q_s \int f_{s,n=0} \delta([\mathbf{R}+\rho] - \mathbf{x}) d^6 Z. \quad (7)$$

Here, $\mathbf{R}+\rho$ is the particle position, $\rho = \mathbf{b}\times\mathbf{v}/\Omega_s$ is the Larmor radius, $d^6Z = m_s^2 B_\parallel^* d\mathbf{R} dv_\parallel d\mu d\alpha$ is the phase space volume of the gyro-center coordinates, $\rho_{ts} = v_{ts}/\Omega_s$ is the Larmor radius evaluated with the thermal velocity $v_{ts} = (T_s/m_s)^{1/2}$, $\lambda_{Ds} = (T_s/4\pi n_s q_s^2)^{1/2}$ is the Debye length, n_s is the density, T_s is the temperature, n is the toroidal mode number, $f_{e,t}$ is a trapped part of the electron distribution function, and α_p is the flux-surface averaged fraction of passing electrons. The gyrokinetic Poisson equation is decomposed into $n\neq 0$ and $n=0$ parts. The former is computed using adiabatic passing electrons and kinetic trapped electrons to avoid the so-called Ω_H mode[39]. Here, a full kinetic electron distribution f_e is computed by Eq. (1), and in Eq. (6), its trapped part $f_{e,t}$ is extracted following a trapped-passing boundary at each position. The latter is solved using full kinetic electrons to satisfy the ambipolar condition, while $\phi_{n=0,m\neq 0}$ convective cells are filtered out from the solution to avoid the Ω_H mode, where m is the poloidal mode number. In the l.h.s., a linear polarization density with a long wavelength approximation, $k_\perp^2\rho_{ts}^2 \ll 1$ is considered, which is valid for ion scale turbulence. The gyrokinetic Poisson operators including the ion polarization density and the adiabatic passing electron density are defined using the initial density and temperature.

The above full-f gyrokinetic model yields the following two balance relations. By taking the time derivative and the flux-surface average of Eq. (7) and substituting Eq. (1), the ambipolar condition is derived as

$$-\sum_s \frac{\rho_{ts}^2}{\lambda_{Ds}^2}\frac{\partial E_r}{\partial t} = 4\pi\sum_s q_s \left\langle f_s(\dot{\mathbf{R}}\cdot\nabla r) - S_{src,s} - S_{snk,s}\right\rangle_{gf}, \quad (8)$$

where E_r is the radial electric field and the gyro/flux-surface average operator is defined as,

$$\langle A\rangle_{gf} = \left\langle \int A(\mathbf{Z})\delta(\mathbf{R}+\rho-\mathbf{x})d^6Z\right\rangle_f, \quad (9)$$

and $\langle\cdot\rangle_f$ is the flux-surface average operator. From the gyrokinetic equation and the Hamilton's equation for the canonical toroidal angular momentum, the toroidal angular momentum balance[32] is given as

$$\begin{aligned}&\left\langle\frac{\partial m_s v_\parallel b_\varphi f_s}{\partial t}\right\rangle_{gf} + \left\langle\frac{1}{\mathscr{J}}\frac{\partial}{\partial\mathbf{R}}\cdot\left(\mathscr{J}\dot{\mathbf{R}}m_s v_\parallel b_\varphi f_s\right)\right\rangle_{gf}\\ &-\left\langle\frac{q_s}{c}f_s\dot{\mathbf{R}}\cdot\nabla\psi\right\rangle_{gf} + \left\langle f_s\frac{\partial\langle\phi\rangle_\alpha}{\partial\varphi}\right\rangle_{gf}\\ &-\left\langle m_s v_\parallel b_\varphi\sum_{s'}C(f_s,f_{s'})\right\rangle_{gf}\\ &-\left\langle m_s v_\parallel b_\varphi(S_{src,s}+S_{snk,s})\right\rangle_{gf} = 0, \end{aligned} \quad (10)$$

where ψ is the poloidal flux, φ is the toroidal angle, and b_φ is the covariant toroidal component of $\mathbf{b}$. Here, the first term is the inertial term, the second term is the stress term, the third term is the radial current term, the fourth term is the toroidal field stress term, the fifth term is the collision term, and the sixth term is the source term. In the stress term, $\dot{\mathbf{R}}$ involve both the magnetic drift $\mathbf{v}_D$ and the $E\times B$ drift $\mathbf{v}_E$, which induce the neoclassical and turbulent Reynolds stress, respectively. Although the neoclassical Reynolds stress is negligible in the axisymmetric limit, it is greatly enhanced in the presence of non-axisymmetric turbulent fluctuations. The radial current term gives the $J\times B$ torque, when summed over all species. This term becomes important in the presence of finite particle transport. The toroidal field stress term is determined by the phase shift between the perturbed density and fluctuating toroidal electric fields, and is also interpreted as the polarization stress[40] or the generalized Maxwell stress[31]. The code has been verified through cross-code comparisons[35,41,42], neoclassical transport[43,44], convergence of E_r up to third order gyrokinetics[32], and multi-species plasma transport[38].

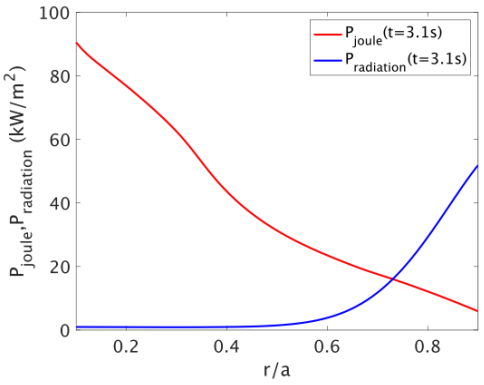

FIG. 3. Radial profiles of the ohmic heating and the radiation loss at $t = 3.1$.

In the numerical experiment, we consider deuterium (D) ions, carbon (C) impurity ions, and kinetic electrons with $m_D/m_e = 3,672$ in a circular concentric tokamak configuration, which is a good approximation for low β plasmas on Tore Supra. The device parameters are $B = 3.7$T, $R_0 = 2.38$m, $a = 0.7$m, $q = 0.76\sim 4.6$, and $P_{joule}\sim 600$kW. The nominal plasma parameters at $r/a = 0.5$ in the LOC phase are $n_e\sim 1.88\times 10^{19}\mathrm{m}^{-3}$, $T_e = 1.54$keV, $T_D = 1.04$keV, $Z_{eff}\sim 3.06$, $\nu_e^*\sim 0.022$, and $\rho^{*-1}\sim 563$. On the other hand, those in the SOC phase are $n_e\sim 3.49\times 10^{19}\mathrm{m}^{-3}$, $T_e = 0.93$keV, $T_D = 0.73$keV, $Z_{eff}\sim 1.36$, $\nu_e^*\sim 0.164$, and $\rho^{*-1}\sim 672$. Here, B is the toroidal magnetic field, R_0 and a are the major and minor radii, r is the radial coordinate, q is the safety factor, P_{joule} is the ohmic heating power, $\nu_e^* \equiv qR_0/(\varepsilon^{3/2}v_{te}\tau_{e,D})$ is the normalized electron collisionality, $\varepsilon = r/R_0$, $\tau_{s,s'}$ is the collision time between the species s and s', and $\rho^* = \rho_{tD}/a$.

Numerical experiments are conducted for $0\le r\le a_0$ to avoid extremely low temperature below 100 eV, where $a_0 = 0.9a$. The boundary conditions of density, rotation, and temperature are given based on the experimental values at $r = a_0$, where rotation and temperature are assumed to be the same between D and C. In the initial condition, density and temperature profiles are given by the experimental data, while rotation profiles are set as rigid rotation with the edge rotation velocity, which is determined mainly by the neoclassical

toroidal viscosity induced by the toroidal ripple, and is almost unchanged through the LOC-SOC transition (see Fig.2(d)). Therefore, the edge rotation velocity is given by an approximate average value over the LOC-SOC transition. By using the same initial rotation profiles and boundary conditions, we compare the formation of intrinsic rotation between the LOC and SOC phases.

According to transport analysis, the radial deposition profiles of the ohmic heating and the radiation loss are given as Fig.3, where the radiation loss makes a dominant contribution to the energy loss ($\sim 75\%$ and $\sim 50\%$ in the LOC and SOC phases, respectively). In this work, the time scale of numerical experiment ~ 10ms is significantly shorter than the time scales of the current diffusion and the particle confinement. Therefore, we do not compute the inductive toroidal electric field, and the resulting ohmic heating and Ware pinch. The ohmic heating is simply modelled as an on-axis electron heating without particle and momentum inputs using a fixed heat source model, $S_{src,s} = \nu_{src,s} A_{src,s}(r)(f_{M1} - f_{M2})$, where $A_{src,s}$ is the deposition profile, f_{M1}, f_{M2} are local Maxwellian distributions with different temperatures, and the heating rate $\nu_{src,s}$ is determined to satisfy the target power input P_{in}. As the electron collision time is sufficiently small $\tau_{ee} \sim 10R_0/v_0$, velocity space perturbations due to the source term is expected to be quickly thermalized, leading to velocity distribution functions relevant for ohmic heating plasmas.

The sink model is somewhat complicated. The heat sink is given by the radiation loss for $r/a > 0.7$ or $r/a_0 > 0.8$. The edge rotation velocity is fixed by the momentum sink due to the neoclassical toroidal viscosity induced by the toroidal ripple. However, the momentum and particle sink due to neutral particles is uncertain, because the detailed distribution of neutral particles was not obtained. In order to model these properties, we implement two sink models. One is a Krook type sink operator $S_{snk1,s} = \nu_{snk1,s} A_{snk1,s}(r)(f_s - f_{0s})$, which gives an effective boundary condition by keeping plasma parameters at the boundary on average. Here, f_{0s} is the initial distribution function, the sink rate is given as $\nu_{snk1,s} = 0.1 v_0/a$, the reference velocity v_0 is given by the thermal velocity of D ions at 1keV, and the deposition profile $A_{snk1,s}$ is localized for $r/a_0 > 0.95$. It is noted that the above sink rate is chosen based on the sensitivity study in Ref. 45. Another is an axisymmetric variant of the Krook type sink operator $S_{snk2,s} = \nu_{snk2,s} A_{snk2,s}(r)(f_{s,n=0} - f_{0s})$, where $\nu_{snk2,s} = 0.01 v_0/a$ and $A_{snk1,s}$ is distributed over $r/a_0 > 0.8$ following the radiation loss profile in Fig.3. The latter model modifies only an axisymmetric part, and a turbulent part is not affected. In addition, the sink parameter is chosen so that $\nu_{snk2,s}$ is sufficiently smaller than the linear growth rates of TEM and ITG, while the sink effect is large enough to avoid deviations of density and temperature profiles from the experimental ones by accumulation of particles and energy induced by plasma transport. These features are important as a sink model distributed over turbulent regions. It is noted that this model also works as a particle source in the outer radii. However, $\nu_{snk2,s}$ is too weak to fix rotation profiles to the initial condition, and rotation profiles freely evolve in this region.

In the numerical experiment, in order to save the computational cost, the plasma size is scaled by a half, and a 1/6 wedge of the torus is computed using 5D grids $(N_R, N_\zeta, N_Z, N_{v\parallel}, N_{v\perp}) = (240, 48, 240, 96, 24)$. The 1/6 wedge torus model is chosen based on the convergence studies in Ref. 46 and in Appendix A. Here, the computational domain in the velocity space is chosen as $-4v_{ts,r=0} \le v_\parallel \le 4v_{ts,r=0}$ and $0 \le \sqrt{2\mu B/m_s} \le 3v_{ts,r=0}$, where $v_{ts,r=0}$ is the thermal velocity at $r = 0$. It is noted that the contrast of temperature is $T_e(r=0)/T_e(r=a_0) \sim 10$ and $T_D(r=0)/T_D(r=a_0) \sim 5$, and the velocity space normalized by the thermal velocity at $r = a_0$ is expanded by ~ 3 times and ~ 2 times, respectively. The velocity grids are chosen to keep sufficient resolution from the core to the edge. GT5D was highly optimized on Fugaku, where a new mixed-precision communication-avoiding Krylov solver enabled efficient computation of kinetic electrons with the real mass ratio[47]. Even with the reduced simulation parameters and the optimization techniques, numerical experiments require costly computation, and a single numerical experiment typically for $\sim 1{,}000R/v_{tD}$ required $\sim 1.5 \times 10^5$ CPU hours on Fugaku[48].

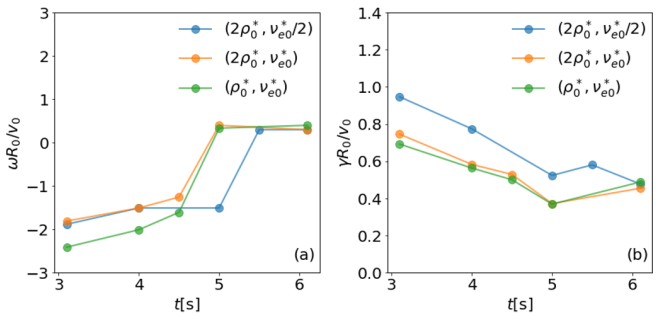

FIG. 4. (a) frequency ω and (b) growth rate γ of TEM and ITG at each time slice in the cases with $(n, \rho^*, \nu_e^*) = (50, \rho_0^*, \nu_{e0}^*)$, $(25, 2\rho_0^*, \nu_{e0}^*)$, and $(25, 2\rho_0^*, \nu_{e0}^*/2)$. $\omega < 0$ is the direction of the electron diamagnetic rotation.

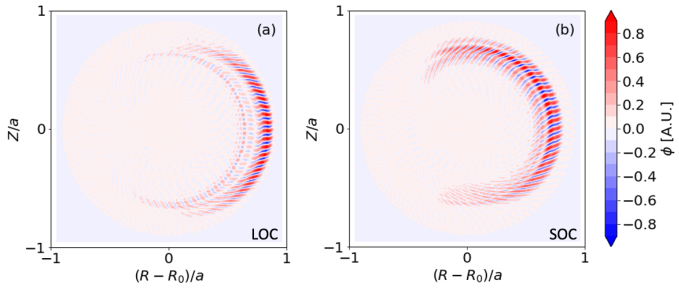

FIG. 5. Linear eigenfunctions $n = 25$ modes at (a) LOC and (b) SOC phases in the case with $\rho^* = 2\rho_0^*$ and $\nu_e^* = \nu_{e0}^*$.

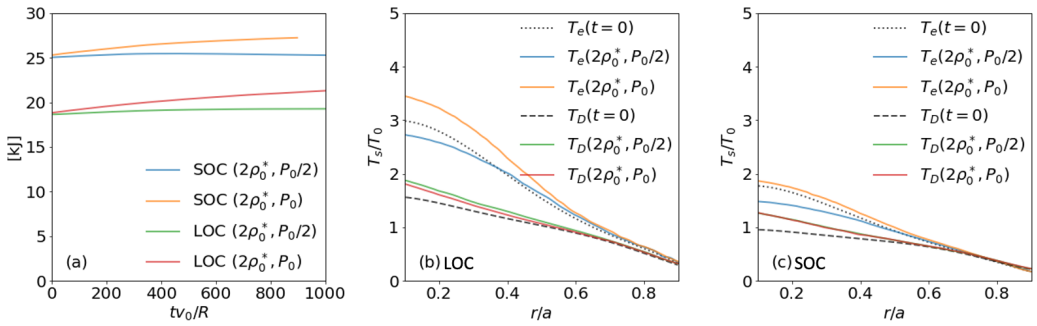

FIG. 6. (a) time history of the stored energy W_t and temperature profiles at $tv_0/R = 800$ in (b) LOC and (c) SOC phases in the cases with $(\rho^*, P_{in}) = (2\rho_0^*, P_0/2)$ and $(2\rho_0^*, P_0)$, respectively. In (b) and (c), the temperature is normalized by $T_0 = 1$keV and dashed and dotted black curves show the initial condition given by the experimental data.

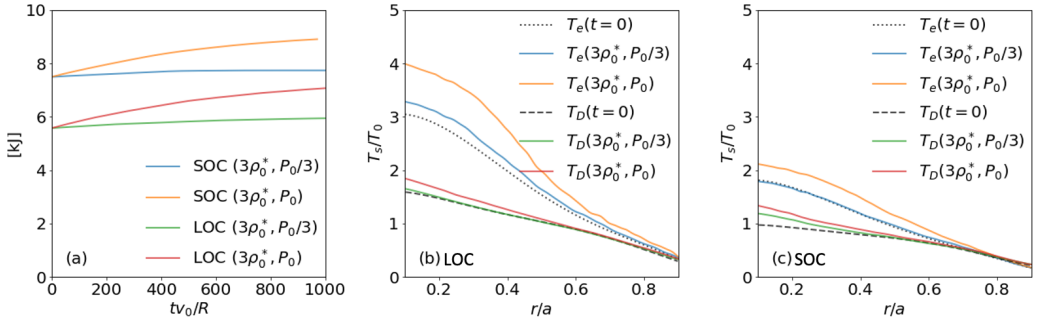

FIG. 7. (a) time history of the stored energy W_t and temperature profiles at $tv_0/R = 800$ in (b) LOC and (c) SOC phases in the cases with $(\rho^*, P_{in}) = (3\rho_0^*, P_0/3)$ and $(3\rho_0^*, P_0)$, respectively. In (b) and (c), dashed and dotted black curves show the initial condition given by the experimental data.

III. VALIDITY OF SCALED PLASMA SIZE

The scaling of the plasma size affects two important non-dimensional parameters, ρ^* and ν_e^*. In this section, we discuss their influences on numerical experiments. Figure 4 shows the frequency and growth rate of $n = 50$ and $n = 25$ modes at each time slice in the cases with $\rho^* = \rho_0^*$ and $\rho^* = 2\rho_0^*$, respectively, where ρ_0^* is the experimental value. As shown in Ref.23, the most unstable modes in the LOC and SOC phases are given by TEM and ITG, respectively. The latter work also showed that in the LOC phase, ITG is stabilized by a dilution effect due to high Z_{eff}, while in the SOC phase, TEM is stabilized by high ν_e^* due to the density ramp. It is noted that in the latter work, local gyrokinetic analyses were conducted at $r/a = 0.37$. However, in Fig.5, global eigenfunctions of both TEM and ITG are peaked in the outer radii. In the experimental parameters, $\rho^* = \rho_0^*$ and $\nu_e^* = \nu_{e0}^*$, the transition from TEM to ITG due to the density ramp occurs at $t = 4.5 \sim 5.0$s. In the experiment, the transition timing was shown to be at $t \sim 4.85$[28]. However, in the 1/2 scale parameters, $\rho^* = 2\rho_0^*$ and $\nu_e^* = \nu_{e0}^*/2$, the transition timing is shifted to $t = 5.0 \sim 5.5$s and the growth rate of TEM is increased by $20 \sim 30\%$. This is attributed to the change of $\nu_e^* \propto R_0$, which characterizes the collisional stabilization effect on TEM. It is noted that the collisional stabilization affects only TEM, and the stability of ITG is similar in all the cases. On the other hand, by doubling the collisionality, the stability of TEM and the transition timing in the experimental parameters are recovered even with the 1/2 scale parameters. Therefore, in this work, we use the modified 1/2 scale parameters, in which the collisionality is adjusted to recover the linear stability in the original experimental parameters.

ρ^* scaling is essentially nonlinear and rather complicated. In the experiment, the confinement scaling was shown to follow the neo-Alcator scaling and the L-mode scaling in the LOC and SOC phases, respectively[1,2]. The latter scaling has Bohm-like ρ^* dependency. On the other hand, according to the derivation of non-dimensional scaling in Ref.49, the former scaling gives gyro-Bohm like ρ^* dependency, while it does not satisfy the so-called Kadomtsev constraint. These controversial ρ^* dependencies between the LOC and SOC phases make the choice of input power difficult in scaled numerical experiments. In terms of the power balance, temperature profiles in a $1/N$ scale plasma become similar to the original ones by imposing the input power of $P_{in} = P_0/N$

and $P_{in} = P_0$, when the energy confinement follows the Bohm scaling and the gyro-Bohm scaling, respectively. Here, P_0 is the input power in the experiment. In order to determine a physically sound heating condition, we conduct power scan numerical experiments with the modified $1/N$ scale parameters, in which the Bohm like heating condition $P_{in} = P_0/N$ and the gyro-Bohm like heating condition $P_{in} = P_0$ are compared. Figures 6 and 7 show the numerical experiments with the modified 1/2 and 1/3 scale parameters, respectively. In Fig.6(a), the stored energy in the Bohm like heating condition is almost unchanged both in the LOC and SOC phases. In Figs.6(b) and 6(c), the electron temperature is higher in the gyro-Bohm heating condition, while the stiff ion temperature is similar in both heating conditions. In Fig.7, these features are more pronounced in the modified 1/3 scale parameters, and the increases of the stored energy and the electron temperature in the gyro-Bohm heating condition are clearly seen. It is noted that in Fig.6 (c), the electron temperature in the Bohm heating condition is lower than the experiment. This is attributed to the modified collisionality, which is increased to satisfy $\nu_e^* = \nu_0$. The SOC phase is characterized by high collisionality, and the increased collisionality leads to stronger ion-electron coupling. The Bohm like scaling in the SOC phase is consistent with the L-mode scaling[1] and our previous works on ρ^* scaling in L-mode plasmas[33,46,50,51]. On the other hand, the Bohm like scaling in the LOC phase may not be consistent with the neo-Alcator scaling. This may be attributed to the lack of Kadomtsev constraint in it. This issue will be addressed in future work. Following the results of the above power scan numerical experiments, in this work, we use the Bohm-like heating condition.

The use of scaled plasma sizes may also affect momentum transport. According to the higher order ballooning theory[52,53], the linear mode asymmetry characterized by the ballooning angle θ_0 is derived as $\theta_0 \propto \rho^{*1/3}$, and the residual stress C_s given by the profile shear stress theory[41] becomes $C_s \propto \rho^{*1/3}$, which is rather weak ρ^* dependency. However, nonlinear gyrokinetic simulations showed much stronger ρ^* dependencies of the residual stress and/or the resulting intrinsic rotation profiles[29,31,33,54,55]. Therefore, the residual stress in scaled numerical experiments may be larger than that in the experiment. However, ρ^* scan numerical experiments typically show similar shapes of intrinsic rotation profiles with different flow velocities[33,55], and thus, at least, the sign relation of rotation changes from the initial rigid rotation is expected to be preserved.

IV. NUMERICAL EXPERIMENT

A. Particle transport

We conduct two numerical experiments in the LOC and SOC phases up to $tv_0/R \sim 1{,}000$ using the modified 1/2 scale parameters with $P_{in} = P_0/2$. Figure 8 shows the radial profiles of the density, the parallel flow, and the temperature at the end of the numerical experiments. The time scale of the numerical experiment is significantly short compared to the particle confinement time, and thus, the electron density is almost unchanged from the initial condition. However, in the LOC phase, where the charge densities of D and C are comparable, the density profiles of D and C respectively show peaking and relaxation, suggesting ion mixing (see Fig.8(a)). As the exhaust of C begins around $t \sim 3$s in Fig.1(a), this result is qualitatively consistent with the experiment. On the other hand, in the SOC phase, where the charge density of C is at the tracer level, this kind of ion mixing does not occur. Figure 9 shows the radial profiles of the radial current. Both in the LOC and SOC phases, the steady ambipolar condition, $\sum_s q_s \langle f_s (\dot{\mathbf{R}} \cdot \nabla r) \rangle_{gf} = 0$, is approximately satisfied. However, the balance of the radial current among three species is quite different between the LOC and SOC phases. In the LOC phase, the D current and the C current greatly exceed the electron current, and they balance with each other, leading to the ion mixing and the exhaust of C. On the other hand, the SOC phase shows a typical ambipolar condition, where the D current is comparable to the electron current and the balance is established mainly by the bulk species.

In the SOC phase, the particle confinement time τ_e and the impurity confinement time τ_C estimated using the volume averaged particle numbers and the particle fluxes at $r/a \sim 0.6$ are respectively $\tau_e \sim 21.4\tau_E$ and $\tau_C \sim 3.4\tau_E$, where τ_E is estimated using the input power and the stored energy at $tv_0/R \sim 1{,}000$ (see Fig.6(a)). The impurity confinement time in the SOC phase is in a similar range as that observed in the tracer impurity injection experiments on Tore Supra[56]. In the LOC phase, the particle and impurity confinement times are estimated as $\tau_e \sim 29.4\tau_E$ and $\tau_C \sim 1.7\tau_E$, respectively. Although this result looks similar to the SOC phase, the impurity content in the LOC phase is at a non-tracer level, $n_C q_C^2 > n_D q_D^2$, and the time scale of inward D flux is also comparable to the impurity confinement time, $\tau_D \sim 2.9\tau_E$, where τ_D is estimated using the absolute value of D flux. This asymmetric electron and D transport with an order of magnitude different particle confinement times suggest fast mixing of ions, leading to the exhaust of C impurity ions.

B. Momentum transport

Figures 8(b) and 8(e) show rotation profiles observed in the numerical experiments. Although the initial condition is given by rigid rotation with the same velocity for both D and C ions, their rotation profiles deviate from the initial condition before the excitation of micro-instabilities. The rotation difference between D and C ions is determined by the neoclassical parallel momentum balance, and is produced by the pressure gradient, leading to the large rotation difference in the outer radii characterized by steep density profiles. This neoclassical effect generates the bootstrap current as shown in the benchmark of the parallel momentum balance between GT5D and the neoclassical theory in Appendix B. Because of this neoclassical effect, an effective boundary condition of the C rotation is deviated from the initial value of $U_C/v_0 \sim -0.05$ to $U_C/v_0 \sim -0.08$. It is noted that the rotation difference is sustained by the collisional parallel momentum exchange be-

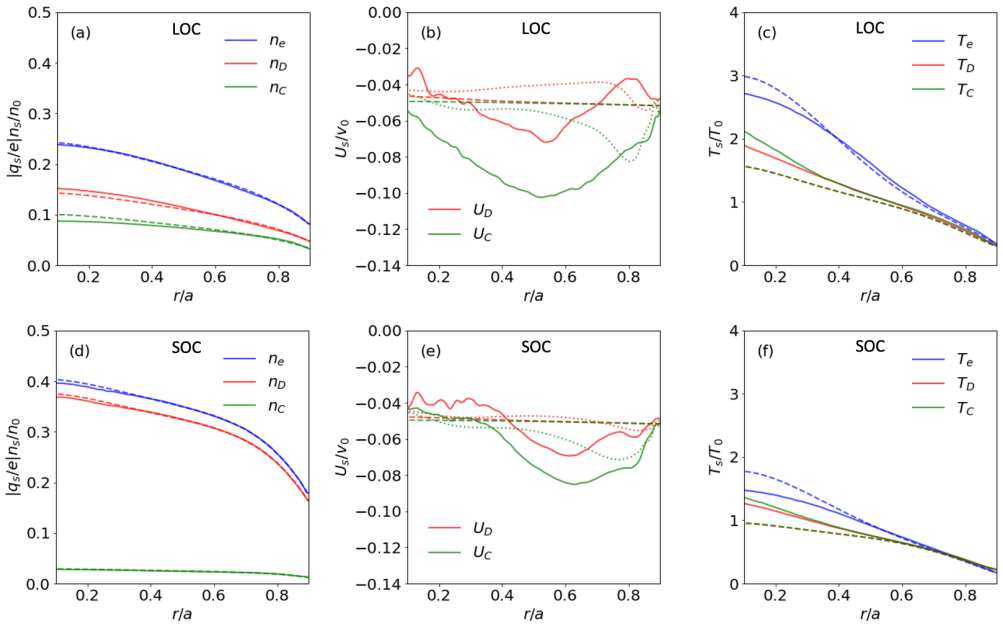

FIG. 8. Radial profiles of (a),(d) the density, (b),(e) the parallel flow, and (c),(f) the temperature averaged over $tv_0/R = 900 \sim 1000$. (a)-(c) and (d)-(f) respectively show the numerical experiments in the LOC and SOC phases. In (a) and (d), the density is normalized by $n_0 = 10^{20}\mathrm{m}^{-3}$. In (a), (c), (d), and (f), dashed curves show the initial profiles given by the experimental data. In (b) and (e), dashed red and green curves show the initial profiles given by rigid rotation, and broken curves show rotation profiles in the neoclassical equilibrium states before the excitation of micro-instabilities ($tv_0/R = 50$).

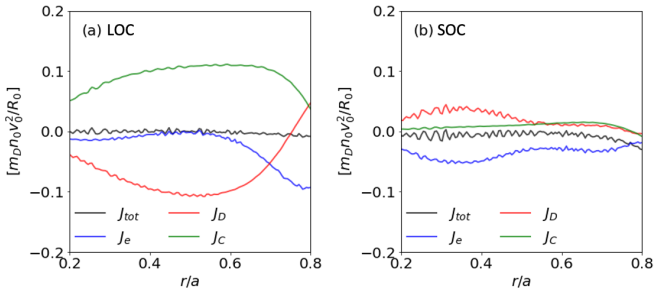

FIG. 9. Radial profiles of the radial current $J_s = \left\langle \frac{q_s}{c} f_s \dot{\mathbf{R}} \cdot \nabla \psi \right\rangle_{gf}$ (the third term in Eq. (10)) averaged over $tv_0/R = 0 \sim 1000$. (a) and (b) respectively show the numerical experiments in the LOC and SOC phases.

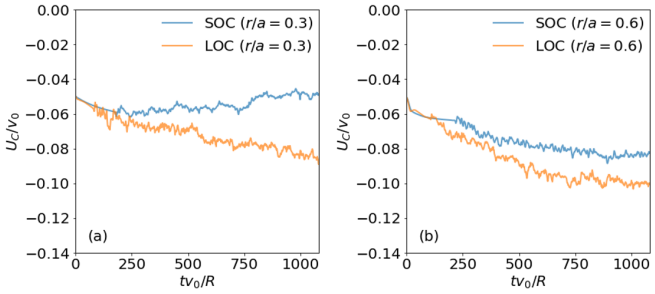

FIG. 10. Time histories of the carbon rotation at (a) $r/a = 0.3$ and (b) $r/a = 0.6$.

tween D and C ions, which is a stronger effect than the radial momentum transport, and thus, the axisymmetric sink $S_{snk2,s}$ with $\nu_{snk2,s} = 0.01 v_0/a$ is too weak to compensate the rotation difference.

The intrinsic rotation shows qualitatively different profiles in the LOC and SOC phases. In the LOC phase, the change of C rotation in the counter-current direction develops globally. Here, the negative direction corresponds to the counter-current direction. On the other hand, in the SOC phase, the change of C rotation in the plasma core is in the co-current direction over significant radii $r/a < 0.5$ with respect to the effective boundary condition. In Fig.10, it is shown that in the plasma core, the intrinsic rotation in the LOC and SOC phases develop in the opposite direction after the initial changes due to the neoclassical effect. In Fig.11, the change of C rotation between the LOC and SOC phases shows a similar radial profile as the experiment.

Although the rotation change is consistent with the experiment, detailed profiles are different from the experimental observation. Figure 12 shows the time evolution of C rotation profiles and a comparison against the experiment. Here, the experimental profiles are shown by interpolated curves

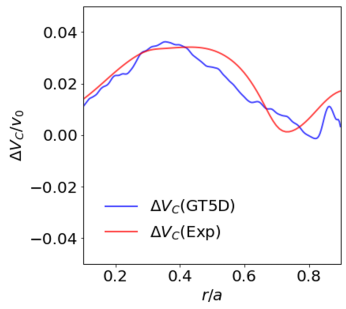

FIG. 11. The change of the carbon rotation between the LOC and SOC phases.

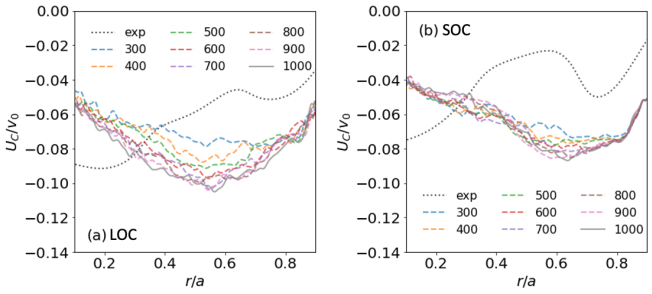

FIG. 12. The carbon rotation profiles at $tv_0/R = 300 \sim 1000$. Black broken curves show the carbon rotation profiles in the experiment. (a) and (b) respectively show the numerical experiments in the LOC and SOC phases.

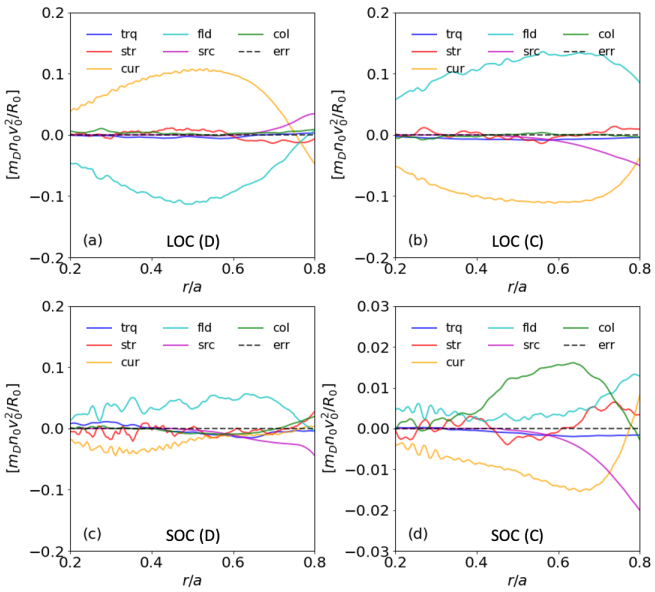

FIG. 13. The toroidal angular momentum balance, Eq. (10), is plotted for (a), (c) D and (b), (d) C. (a), (b) and (c), (d) respectively show the numerical experiments in the LOC and SOC phases. The radial profiles of the inertial term (trq, the first term), the stress term (str, the second term), the radial current term (cur, the third term), the toroidal field stress term (fld, the fourth term), the collision term (col, the fifth term), the source term (src, the sixth term), and the remaining error (err) are averaged over $tv_0/R = 0 \sim 1000$.

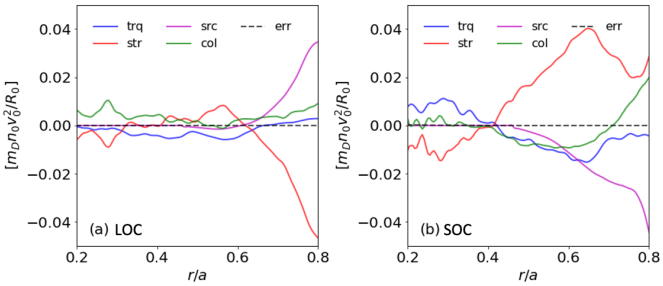

FIG. 14. The gyrokinetic equation part of the toroidal angular momentum balance, Eq. (11), is plotted for D. (a) and (b) respectively show the numerical experiments in the LOC and SOC phases. The radial profiles of the inertial term (trq, the first term), the partial stress term (str, the second term), the collision term (col, the third term), the source term (src, the fourth term), and the remaining error (err) are averaged over $tv_0/R = 0 \sim 1000$.

for simplicity. Although the rotation profiles are still slowly evolving in time, qualitative features of profile shapes are unchanged. Both in the LOC and SOC phases, the C rotation profiles are shifted in the counter-current direction, because of the deviation of effective boundary conditions due to the neoclassical effect. In the LOC phase, the positive C rotation gradient U_C' in the outer radii (U_C' averaged over $r/a = 0.5 \sim 0.8$ is $U_C' a/v_0 \sim 0.085$) is in a similar range as the experiment (U_C' averaged over $r/a = 0.3 \sim 0.9$ is $U_C' a/v_0 \sim 0.081$). In the SOC phase, the negative rotation gradient around the mid radius (U_C' averaged over $r/a = 0.4 \sim 0.6$ is $U_C' a/v_0 \sim -0.13$) is still weaker than the experiment (U_C' averaged over $r/a = 0.6 \sim 0.7$ is $U_C' a/v_0 \sim -0.23$), and the position of negative rotation gradient is shifted from $r/a \sim 0.65$ to $r/a \sim 0.5$. Both in the LOC and SOC phases, the rotation gradients in the plasma core are opposite from the experiment, which may be attributed to the sawtooth activity inside the sawtooth inversion radius ($r/a \sim 0.25$)[14].

In order to understand these intrinsic rotation profiles, the toroidal angular momentum balance (10) is analyzed. In Fig.13, the toroidal angular momentum balance is dominated by the radial current term and the toroidal field stress term, and the origin of the inertial term is not clearly seen. It is noted that the balance between the radial current term and the toroidal field stress term indicates that the ion mixing is produced by the toroidal field stress term. In order to investigate the origin of the inertial term in detail, we remove the contributions from the radial current term and the toroidal field term by decomposing the toroidal angular momentum balance (10)

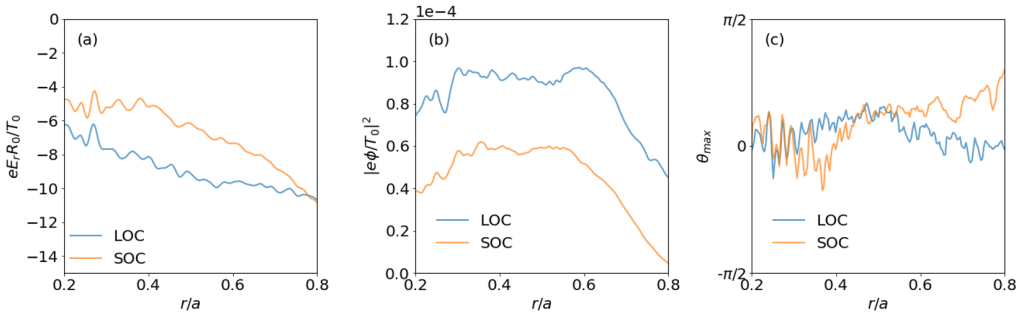

FIG. 15. Comparisons of radial profiles of (a) radial electric field E_r, (b) turbulent intensity $|e\phi/T_0|^2$, and (c) poloidal angle at the maximum turbulent intensity θ_{max} between the LOC ans SOC phases. The profiles are averaged over $tv_0/R = 0 \sim 1000$.

into the gyrokinetic equation part,

$$\left\langle \frac{\partial m_s v_\parallel b_\varphi f_s}{\partial t} \right\rangle_{gf} + \left\langle \frac{m_s v_\parallel b_\varphi}{\mathscr{J}} \frac{\partial}{\partial \mathbf{Z}} \cdot \left(\mathscr{J} \dot{\mathbf{Z}} f_s \right) \right\rangle_{gf} - \left\langle m_s v_\parallel b_\varphi \sum_{s'} C(f_s, f_{s'}) \right\rangle_{gf} - \left\langle m_s v_\parallel b_\varphi (S_{src,s} + S_{snk,s}) \right\rangle_{gf} = 0, \quad (11)$$

and the Hamilton's equation part,

$$\left\langle \frac{f_s}{\mathscr{J}} \frac{\partial}{\partial \mathbf{Z}} \cdot \left(\mathscr{J} \dot{\mathbf{Z}} m_s v_\parallel b_\varphi \right) \right\rangle_{gf} - \left\langle \frac{q_s}{c} f_s \dot{\mathbf{R}} \cdot \nabla \psi \right\rangle_{gf} + \left\langle f_s \frac{\partial \langle \phi \rangle_\alpha}{\partial \varphi} \right\rangle_{gf} = 0, \quad (12)$$

following the derivation in Ref.32. Figure 14 shows the gyrokinetic equation part of the toroidal angular momentum balance, in which the inertial term is determined by the partial stress term, the collision term, and the source term. Except for the outer radii, where the source term becomes large, the inertial term is mainly correlated with the partial stress term, which is determined by plasma turbulence, while the collisional momentum exchange between D and C is non-negligible in the LOC phase. Therefore, we further investigate properties of turbulent momentum transport based on the mechanisms reviewed in Refs.57 and 58. It is noted that the source term develops in the opposite direction in the outer radii. In the numerical experiment, the momentum source is given by the Krook type sink models, $S_{snk,s1}$ and $S_{snk,s2}$, in which the sign of momentum source is determined in a passive manner by turbulent momentum transport. Therefore, turbulent momentum transport leads to the opposite net torque input between the LOC and SOC phases.

In the framework of local turbulence theory, the momentum flux Π_s may be decomposed as

$$\Pi_s = n_s m_s R_0 \left[-\chi_{\varphi,s} R_0 \Omega'_{\varphi,s} + V_{\varphi,s} R_0 \Omega_{\varphi,s} + C_s \right], \quad (13)$$

where $\Omega_{\varphi,s}$ is the toroidal angular frequency, $\Omega'_{\varphi,s} = \partial \Omega_{\varphi,s}/\partial r$, $\chi_{\varphi,s}$ is the momentum diffusion coefficient, $V_{\varphi,s}$ is the pinch velocity, and C_s is the residual stress including various symmetry breaking effects. Here, the residual stress comes mainly from the plasma shaping effect C_{PS}[59], the profile shear $C_{\rho*}$[41], the E_r shear C_E[60,61], and the turbulence intensity gradient C_I[62]. The symmetry breaking due to plasma shaping does not exist in the current circular concentric tokamak configuration. In Fig.15(a), the radial electric field E_r has negative shear on average, and the momentum transport due to the E_r shear stress $C_E \propto -dE_r/dr$ is expected to be outward both in the LOC and SOC phases. In Fig.15(b), the turbulent intensity $I = |e\phi/T_0|^2$ shows similar profiles, which have flat profiles for $r/a = 0.3 \sim 0.6$ and negative gradients for $r/a > 0.6$, and the momentum transport induced by the turbulent intensity shear stress $C_I \propto dI/dr$ seems to be similar between the LOC and SOC phases. It is noted that the turbulent intensity normalized by T_0 becomes smaller in the edge, where temperature becomes lower. However, $|e\phi/T_e|$ and $|\delta n_e/n_e|$ increases towards the edge. Finally, in Fig.15(c), an approximate ballooning angle θ_{max}, which is given by the poloidal angle at the maximum turbulent intensity within each magnetic surface, shows qualitative difference between the LOC and SOC phases. In the outer radii, θ_{max} in the LOC phase is slightly negative, while θ_{max} in the SOC phase is positive. The sign relation of the profile shear stress $C_{\rho*} \propto -\theta_0 \sim \theta_{max}$ is consistent with the change of intrinsic rotation between the LOC and SOC phases.

The normalized profile shear stress is given as[41]

$$\frac{R_0 C_{\rho*,s}}{v_{ts} \chi_{\varphi,s}} = -\frac{\hat{s}\theta_0}{2|q|k_\theta \rho_{ts}} \left(\frac{R_0}{L_{n,s}} + 4 - \frac{1}{(\sqrt{2} q k_\theta \rho_{ts})^2} \right), \quad (14)$$

where θ_0 is the ballooning angle, $\hat{s}$ is the magnetic shear, k_θ is the poloidal wavenumber, and $L_{n,s} = |n_s/\nabla n_s|$ is the density gradient scale length. Here, the mode asymmetry θ_0 and the corresponding linear growth rate γ are given by the higher order ballooning theory[52,53] as,

$$\theta_0 = -sign\left(\hat{s}\omega'_r\right) \left| \frac{\omega'_r}{2k_\theta \gamma_0 \hat{s}} \right|^{1/3}, \quad (15)$$

$$\gamma = \gamma_0 \cos(\theta_0), \quad (16)$$

where γ_0 is the linear growth rate without mode asymmetry, ω_r is the mode frequency, and $\omega'_r = \partial \omega_r/\partial r$. Although Ref.41

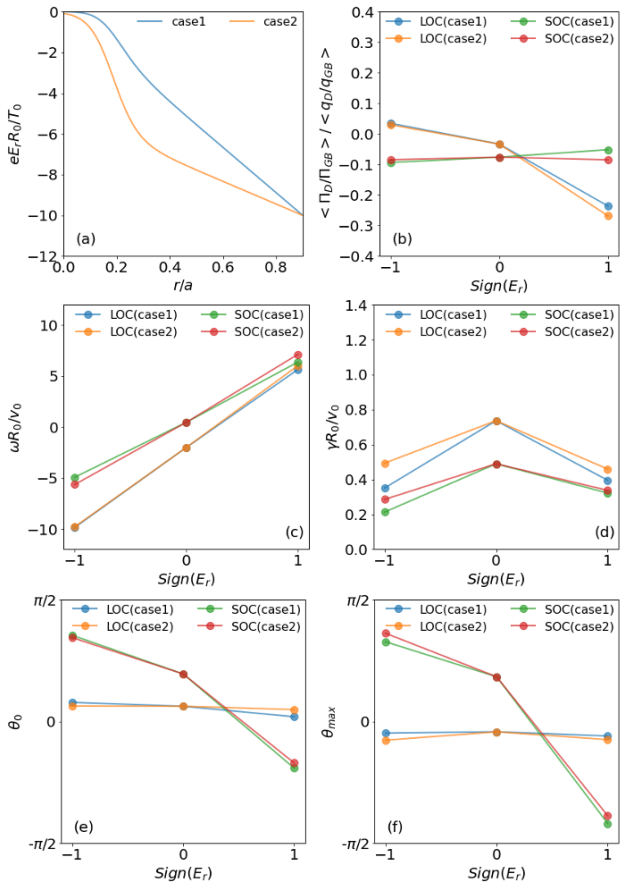

FIG. 16. Linear calculations of $n = 25$ modes of TEM in the LOC phase and ITG in the SOC phase with externally imposed positive and negative E_r. (a) shows the radial profiles of E_r used in case 1 and case 2. (b) shows the volume averaged quasilinear flux ratio between turbulent heat and momentum transport. The heat and momentum fluxes are respectively normalized by $q_{GB} = \chi_{GB} n_0 T_0/a$ and $\Pi_{GB} = \chi_{GB} n_0 v_0/a$, where $\chi_{GB} = (v_0^3/\Omega_D^2)/a$. (c) and (d) show the frequency and the growth rate, respectively. (e) and (f) shows the ballooning angle θ_0, which is defined at the minimum radial wavenumber k_r, and an approximate ballooning angle, which is given at the maximum amplitude of ϕ, respectively.

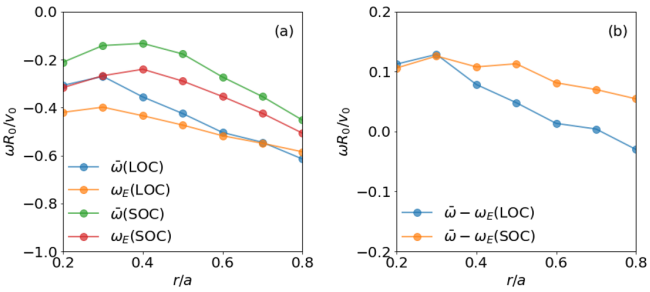

FIG. 17. (a) shows the weighted turbulence frequency $\bar{\omega}$ and the Doppler shift due to $E \times B$ rotation ω_E of $n = 24$ modes at each radius. (b) shows of the frequency of $n = 24$ modes corrected by subtracting the Doppler shift, $\bar{\omega} - \omega_E$. The frequency spectra are obtained from the time series data for $tv_0/R = 600 \sim 1000$.

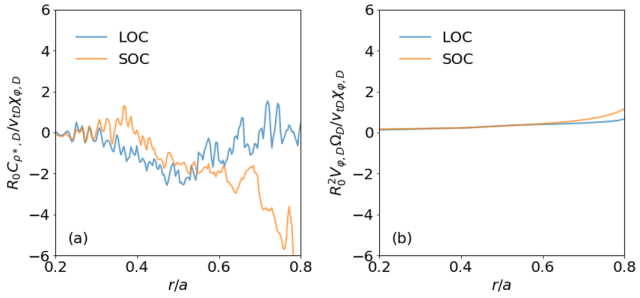

FIG. 18. Radial profiles of (a) the normalized profile shear residual stress $R_0 C_{\rho*,D}/v_{tD}\chi_{\varphi,D}$ and (b) the normalized curvature pinch $R_0^2 V_{\varphi,D}\Omega_D/v_{tD}\chi_{\varphi,D}$. The plasma profiles are given by the simulation data in Fig.8. In estimating the profile shear stress, $k_\theta \rho_D = 0.35$ is assumed, and θ_0 is given by θ_{max} in Fig.15(c).

discussed the profile shear stress without E_r, the higher order ballooning theory can be naturally extended including the E_r shear[63,64]. Therefore, the profile shear stress involves the E_r shear stress, when the mode asymmetry is affect also by E_r. In Ref.45, the profile shear stress including E_r was analyzed for ITG with adiabatic electrons using linear global calculations with externally imposed E_r, and the relation between the E_r shear and the profile shear stress was clarified.

In this work, we apply this approach to TEM in the LOC phase and ITG in the SOC phase to understand the change of θ_0 between the LOC and SOC phases. Based on the E_r profiles in Fig.15(a), model E_r profiles are chosen as $eE_rR_0/T_0 = sign(E_r)(c_0 + c_1 r/a_0)(\tanh[(r/a_0 - 0.2)/0.1] + 1)/2$ with $(c_0, c_1) = (0, 10)$ (case 1) and $(5, 5)$ (case 2), in which E_r at the outer radii becomes similar but the E_r shear differ by two times (see Fig.16(a)). In Fig.16, (b) the volume averaged quasi-linear flux ratio between turbulent heat and momentum transport, (c) the frequency, (d) the growth rate, (e) the ballooning angle θ_0 defined by the poloidal angle at the minimum radial wavenumber k_r, and (f) the approximate ballooning angle θ_{max} defined by the poloidal angle at the maximum amplitude of ϕ are shown for case 1 and case 2 with negative and positive E_r. It is noted that linear calculations with E_r show oscillatory linear growth, which is a typical feature of the so-called Floquet ballooning mode[65], and the above results are time averaged. In Fig.16(c), the frequencies of both TEM and ITG are affected by the Doppler shift, and become the same sign as in the numerical experiment. Here, case 1 and case 2 give almost the same frequencies, because they have similar E_r. In Fig.16(e), the changes of θ_0 are similar between case 1 and case 2, while the theory predicts $\theta_0 \propto \omega_r'^{1/3}$. This result suggests that θ_0 is determined not only by the E_r shear but also by E_r itself. This feature was observed also in Refs.45 and 64. Accordingly, in Fig.16(d), the

stabilization effect due to E_r becomes similar between case 1 and case 2. Another important finding is that TEM in the LOC phase shows much smaller change of θ_0 than ITG in the SOC phase. This may be attributed to the higher linear growth rate and the narrower mode width of TEM in the LOC phase. In Fig.16(f), TEM in the LOC phase and ITG in the SOC phase respectively show slightly negative θ_{max} and positive θ_{max} at the negative E_r, which is consistent with the numerical experiment (see Fig.15(c)). In Fig.16(b), the resulting momentum transport at the negative E_r becomes outward and inward in the LOC and SOC phases, respectively.

In Fig.17(a), the weighted turbulence frequency $\bar{\omega}(r,n) = \sum_\omega \omega|\hat{\phi}_{n,\omega}|^2/\sum_\omega|\hat{\phi}_{n,\omega}|^2$ of $n=24$ mode at each radius is in the electron diamagnetic direction over the whole radii, where $\hat{\phi}_{n,\omega}$ is the Fourier component of ϕ at $\theta=0$ with respect to the toroidal mode number n and the frequency ω. However, if one corrects the frequency by subtracting the Doppler shift of poloidal $E\times B$ rotation due to the radial electric field $\omega_E = k_\theta v_{E\theta}$, the LOC and SOC phases show qualitatively different properties, where $v_{E\theta} = \langle \mathbf{v}_E\cdot\nabla\theta/|\nabla\theta|\rangle_f$. The SOC phase is characterized by the positive frequency or ITG over the whole radii. On the other hand, the LOC phase shows ITG only in the plasma core, and the outer radii are characterized by the negative frequency or TEM. These results show that the different features of the mode asymmetry between TEM in the LOC phase and ITG in the SOC phase, which depend not only on the profile shear and the E_r shear but also on E_r itself, are key physics in understanding the change of intrinsic rotation during the LOC-SOC transition.

Finally, we compare the relative magnitude of the profile shear stress against the Coriolis pinch given as[57],

$$\frac{R_0^2 V_{\varphi,s}\Omega_s}{v_{ts}\chi_{\varphi,s}} = \left(-\frac{4T_s}{T_e}-\frac{R_0}{L_n}\right)\frac{R_0\Omega_s}{v_{ts}}. \qquad (17)$$

Figure 18 shows (a) the normalized profile shear stress and (b) the normalized Coriolis pinch, where the plasma profiles are given by the simulation data in Fig.8. In estimating the profile shear stress, $k_\theta\rho_{tD}=0.35$ is assumed and the mode asymmetry is given by θ_{max} in Fig.15(c). The Coriolis pinch is outward both in the LOC and SOC phases, and is negligible for the intrinsic rotation with the low Mach number. The negligible impact of the Coriolis pinch was also shown in Ref. 20.

C. Energy transport

In Figs.8(c) and 8(f), T_e in the plasma core is slightly lower than the experiment, while T_D and T_C are slightly higher than the experiment. As already discussed, the increased collisionality leads to stronger ion-electron coupling, and the difference between T_e and T_D in the plasma core becomes smaller than the experiment. Figure 19 shows the surface integrated energy flux $Q_s = \hat{Q}_s S$ observed in the quasi-steady phase of the numerical experiments, where $\hat{Q}_s \equiv \langle\int[m_s v_\parallel^2+\mu B]f_s(\mathbf{v}_D+\mathbf{v}_E)\cdot\nabla r d^3v\rangle_f$ is the energy flux density and $S=2\pi r R_0$. In the current numerical experiments, the deposition profiles of the ohmic heating and the radiation loss overlap with each other

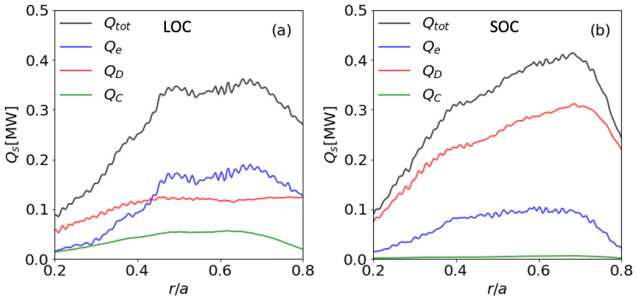

FIG. 19. Radial profiles of the surface integrated energy flux Q_s averaged over $tv_0/R = 900\sim1000$. (a) and (b) respectively show the numerical experiments in the LOC and SOC phases.

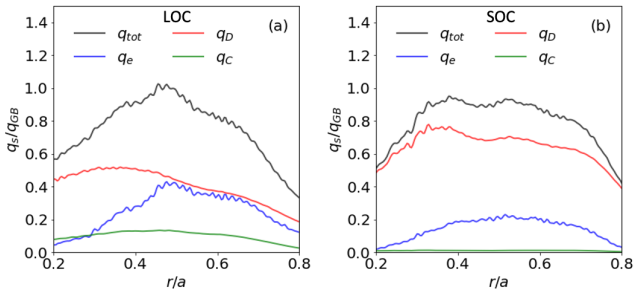

FIG. 20. Radial profiles of the heat flux density q_s averaged over $tv_0/R = 900\sim1000$. (a) and (b) respectively show the numerical experiments in the LOC and SOC phases.

(see Fig.3), and a source free region does not exist. Therefore, both in the LOC and SOC phases, the total energy flux slightly exceeds the input power of $P_{in}=P_0/2=300$kW, while the stored energy is in the quasi-steady state (see Fig.7(a)). In the LOC phase, the electron energy flux is dominant, while both the D and C energy fluxes make significant contributions. On the other hand, in the SOC phase, the D energy flux is dominant, and the C energy flux is negligible. These results are qualitatively consistent with the experiment and the local gyrokinetic analyses in Ref.23, while several differences are not captured in the current numerical experiments.

Figure 20 shows the heat flux density $q_s = \hat{Q}_s - 5/2T_s\Gamma_s$, where $\Gamma_s \equiv \langle\int f_s(\mathbf{v}_D+\mathbf{v}_E)\cdot\nabla r d^3v\rangle_f$ is the particle flux density. In Ref.23, the power balance analysis at $r/a=0.37$ gave the ion and electron heat fluxes of $(q_i,q_e) = (4.5\pm1.0\text{kWm}^{-2}, 6.7\pm1.0\text{kWm}^{-2})$ and $(q_i,q_e) = (14.0\pm3.0\text{kWm}^{-2}, -1.0\pm3.0\text{kWm}^{-2})$ in the LOC and SOC phases, respectively. However, in the LOC phase shown in Fig.20(a), the ion heat fluxes q_D+q_C exceeds q_e at $r/a=0.37$. In the SOC phase shown in Fig.20(b), we do not observe the electron heat pinch over the whole radii. The detailed ratios between the ion and electron energy fluxes may be affected either by the enhanced ion-electron coupling and by the modelling of sources and sinks. On the other hand, the mechanism of the

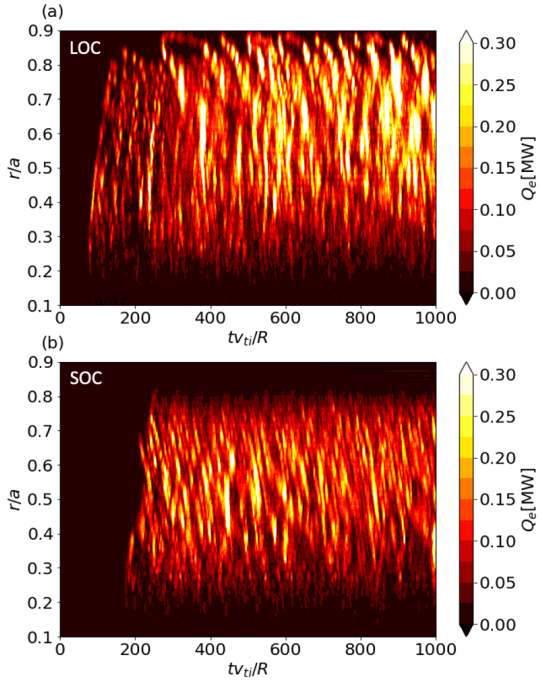

FIG. 21. Spatio-temporal evolution of the electron energy flux in (a) LOC and (b) SOC phases.

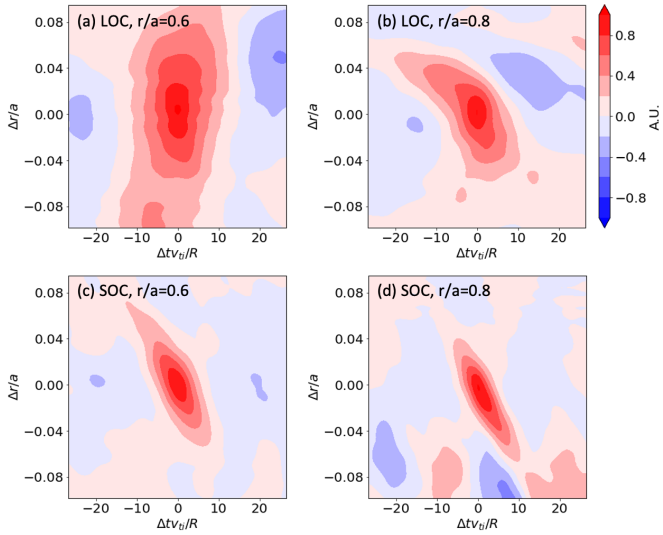

FIG. 22. Spatio-temporal auto-correlation functions of the electron energy flux evaluated for (a) LOC phase, $r/a = 0.6$, (b) LOC phase, $r/a = 0.8$, (c) SOC phase, $r/a = 0.6$, and (d) SOC phase, $r/a = 0.8$. Δt and Δr respectively show delays in time and radius. The electron energy flux data in Fig.21 is processed for $tv_0/R = 400 \sim 1000$.

electron heat pinch is still an open issue. It is noted that in Ref.66, off diagonal terms in the transport matrix was derived for the curvature pinches, where an Onserger symmetrical contribution to the heat flux gives heat pinch when off-diagonal particle pinch occurs.

Figures 21 and 22 show the spatio-temporal evolution of the electron energy flux and the corresponding spatio-temporal auto-correlation functions. Both the LOC and SOC phases are characterized by bursts of avalanche like nonlocal transport, while their dynamics is somewhat different. The SOC phase is characterized by ballistic inward propagation of global avalanches from the edge to the core. This feature is clearly seen by the spatio-temporal autocorrelation functions in Figs. 22(c) and 22(d). In Ref.36, it was shown that the direction of the avalanche propagation in ITG turbulence is determined by the asymmetry induced by the E_r shear, which results in the inward and outward propagation with the negative and positive E_r shear, respectively. The inward propagation of avalanches is consistent with the negative E_r shear in Fig.15(a). On the other hand in the LOC phase, the propagation width is limited, and avalanches show discontinuities around $r/a = \sim 0.7$. In Fig.22 (b), the spatio-temporal autocorrelation function at $r/a \sim 0.8$ shows that inward propagation of avalanches is limited and the correlation length becomes shorter inside $r/a \sim 0.8$, while in Fig.22(a), the spatio-temporal autocorrelation function at $r/a \sim 0.6$ suggest global mode structures with small time delay. This may be attributed to the change of dominant turbulence drive from ITG to TEM, which was shown in Fig.17(b).

D. Quasi-coherent modes

Figures 23(a) and 23(c) show the frequency spectra of the electrostatic potential measured at $\theta = 0, \varphi = 0$, and $r/a = 0.7$. Since the spectrum is symmetric with respect to the sign of frequency, only the negative frequency part is plotted. Here, $r/a = 0.7$ is characterized by TEM and ITG in the LOC and SOC phases, respectively (see Fig.17(b)). The spectrum in the LOC phase shows a few quasi-coherent peaks, which were called as the quasi-coherent modes (QCMs). On the other hand, the SOC phase is characterized by a broad-band spectrum without such coherent peaks. These spectra are qualitatively consistent with those in the experiment[28], while the peak positions of QCMs are different. In the experiment, the QCM peak appeared in the 50kHz range, which correspond to $\omega R/v_0 \sim 0.5$. Although the secondary peak with $n = 18$ is in this range, the primary peak appear in the lower frequency range. This difference may be attributed to the magnetic ripples, which can enhance E_r and the resulting Doppler shift[69].

Figures 23(b) and 23(d) show the frequency spectrum of each n component measured at $\theta = 0$ and $r/a = 0.7$, which is non-symmetric with respect to the sign of frequency because of the resonance condition depending on n. It is noted that $\bar{\omega}$ in Fig.17 is estimated by the weighted average using the $n = 24$ spectrum. The n spectra clearly show the structures of the QCMs and the broad-band fluctuations, which have the following features. Firstly, the width of each n spectrum is narrower in the LOC phase. The half height width of the $n = 12$ spectrum is estimated as $\sim 0.035 v_0/R$ and $\sim 0.065 v_0/R$ in the LOC and SOC phases, respectively. This may be attributed to the difference of nonlinear spectral broad-

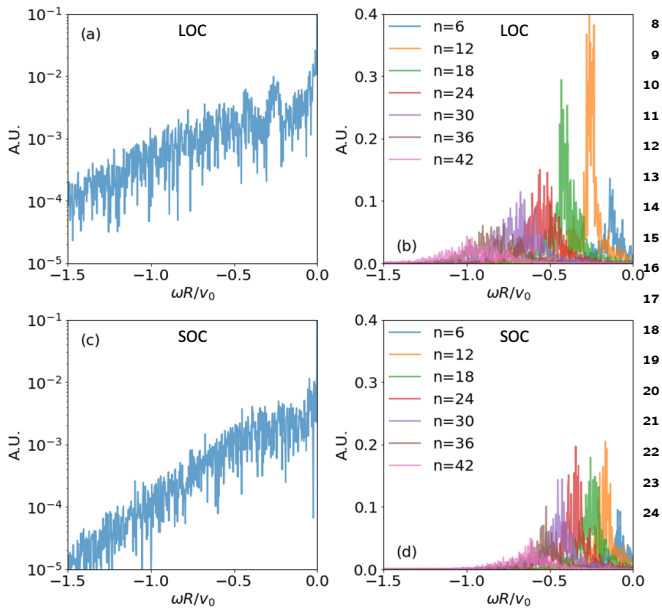

FIG. 23. Frequency spectra of (a),(c) the electrostatic potential measured at $(r,\theta,\varphi)=(0.7a,0,0)$, $|\hat{\phi}_{\omega}|$, and (b),(d) the toroidal mode number component of the electrostatic potential measured at $(r,\theta)=(0.7a,0)$, $|\hat{\phi}_{\omega,n}|$. (a),(b) and (c),(d) respectively show the numerical experiments in the LOC and SOC phases. The frequency spectra are obtained from the time series data for $tv_0/R=600\sim1000$.

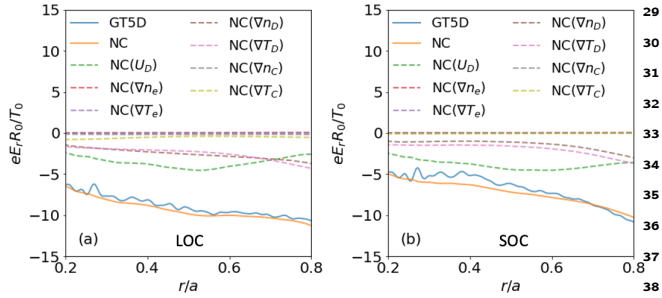

FIG. 24. Radial profiles of E_r observed in the numerical experiment (GT5D) and E_r estimated by the parallel momentum balance based on the Hirshman-Sigmar's moment approach (NC)[67,68]. The D component of the parallel momentum balance is computed using the D parallel flow U_D, the density n_s, and the temperature T_s from GT5D, and terms proportional to U_D and the gradients of n_s and T_s are also shown. Both E_r and the plasma profiles are averaged over $tv_0/R=0\sim1000$. (a) and (b) respectively show the numerical experiments in the LOC and SOC phases.

ening between TEM and ITG. Secondly, the frequency gap of peaks in the n spectra is larger in the LOC phase. The mode frequency with the Doppler shift is given by $\omega_{shift}=\omega+k_\theta v_{E\theta}\sim(nq/r)(v_{ph}+v_{E\theta})$, and the frequency gap between adjacent n modes becomes $\Delta\omega_{shift}=(q/r)(v_{ph}+v_{E\theta})$, where $v_{ph}=\omega/k_\theta$ is the phase velocity. As shown in Fig.17(a), both in the LOC and SOC phases, the Doppler shift is in the electron diamagnetic direction, $v_{E\theta}<0$, and the frequencies of TEM and ITG are shifted in the electron diamagnetic direction. On the other hand, the phase velocity of TEM and ITG are in the electron diamagnetic direction, $v_{ph}<0$, and in the ion diamagnetic direction, $v_{ph}>0$, respectively. In addition, the magnitude of $v_{E\theta}$ becomes larger in the LOC phase. Therefore, the frequency gap becomes larger in the LOC phase. Because of these two features, the n spectra in the LOC phase split to form the QCMs. It is noted that in Ref.23, the former effect was shown, while the latter effect was not taken into account, because the simulation was conducted using a local δf gyrokinetic model without E_r.

In Fig.24, E_r observed in the numerical experiment is compared against the neoclassical theory. By substituting the D parallel flow U_D, the density n_s, and the temperature T_s from GT5D for the D component of the parallel momentum balance (B7), E_r is written as

$$E_r=-\frac{1}{A_{21}+A_{22}+A_{23}}\left[\frac{|\nabla\psi|}{F}\langle BU_D\rangle_f -A_{21}\frac{T_e}{q_e}\frac{\partial\ln p_e}{\partial r}-A_{22}\frac{T_D}{q_D}\frac{\partial\ln p_D}{\partial r}-A_{23}\frac{T_C}{q_C}\frac{\partial\ln p_C}{\partial r} +A_{24}\frac{T_e}{q_e}\frac{\partial\ln T_e}{\partial r}+A_{25}\frac{T_D}{q_D}\frac{\partial\ln T_D}{\partial r}+A_{26}\frac{T_C}{q_C}\frac{\partial\ln T_C}{\partial r}\right], \quad (18)$$

where F is the toroidal flux, $p_s=n_sT_s$ and A_{ij} is given by elements of the matrix $\mathbf{A}=(\mathbf{L}-\mathbf{M})^{-1}\cdot\mathbf{M}$ (see Appendix B for detailed definitions). In Fig.24, the dominant contributions come from the parallel flow, the density gradient of D, and the temperature gradient of D. It is noted that because of the charge dependency, the contribution from C is negligible even in the LOC phase. The contributions from the density and temperature gradients are larger in the LOC phase, reflecting the higher temperature. On the other hand, the largest contribution comes from the counter-current rotation, and its magnitude is comparable between the LOC and SOC phases, because the boundary condition or the baseline rotation is determined by the toroidal ripple. The large negative E_r induced by the ripple induced counter-current rotation is a unique feature on Tore Supra[69,70].

V. SUMMARY

In this work, we analyzed Tore Supra ohmic L-mode discharge 48102 focusing on two time slices in the LOC and SOC phases using the global full-f gyrokinetic Eulerian code GT5D. Because of limited computational resources, the numerical experiments were conducted using the modified 1/2 scale parameters, in which the plasma size is reduced by a half, while the collisionality is enhanced to keep the experimental value of ν_e^*. The modified 1/2 scale parameters keep the stability of TEM in the original experimental parameters. However, collisional ion-electron coupling becomes stronger, leading to smaller temperature difference between ions and electrons. The heating condition was chosen based on power scans using the modified 1/2 and 1/3 scale parameters. The

power scan numerical experiments showed the Bohm like scaling both in the LOC and SOC phases, and the Bohm like heating condition, in which the input power is scaled as proportional to the plasma size, was adopted in the numerical experiments. The Bohm like scaling is consistent with the L-mode scaling observed in the SOC phase, while its relevance in the LOC phase, which is characterized by the neo-Alcator scaling, is still an open issue.

The numerical experiments captured qualitative features of transport phenomena in the LOC-SOC transition on Tore Supra. Firstly, the exhaust of C is induced by the ion mixing, which is driven by the toroidal field stress. Secondly, the intrinsic rotation develops in the opposite directions between the LOC and SOC phases, which is characterized by the different features of TEM in the LOC phase and ITG in the SOC phase, leading to the change of the profile shear stress. Here, the mode asymmetry or the ballooning angle depends not only on the profile shear and the E_r shear but also on E_r itself. It is noted that although the rotation change is reproduced, detailed intrinsic rotation profiles are still different from the experiment, and further investigations on momentum source and sink models are needed. Thirdly, the ratio of the stored energy between two time slices and the temperature profiles in the experimental data are approximately recovered in the quasi-steady state, where the energy fluxes of electrons and D are dominant in the LOC and SOC phases, respectively. Finally, turbulent spectra in the LOC and SOC phases are characterized by QCMs and broad-band spectra, which are produced by the difference of Doppler shift in the LOC and SOC phases. The ripple induced counter-current rotation produce the Doppler shift in the electron diamagnetic direction, which enhances the frequency gap of each n spectrum, leading to QCMs.

As already discussed, further studies are required to understand ρ^* scaling in the LOC phase. Although Tore Supra showed the change of intrinsic rotation in the co-current direction during the LOC-SOC transition, many other devices showed the change of intrinsic rotation in the opposite direction[2]. Another important issue is the change of nonlocal transport between the LOC and SOC phases, which was experimentally observed by applying edge cold pulses[2]. In future work, these important issues will be addressed using global full-f gyrokinetic simulations.

ACKNOWLEDGMENTS

This work was supported by the MEXT Japan (Program for Promoting Researches on the Supercomputer Fugaku "Exploration of Burning Plasma Confinement Physics", and Grant No.22K03584) and the NIFS Collaborative Research Program (NIFS16KNST103). This research used computational resources of the supercomputer Fugaku provided by the RIKEN Center for Computational Sciences (hp210178,hp220165), and the ICEX provided by the JAEA.

DATA AVAILABILITY STATEMENT

The data that support the findings of this study are available from the corresponding author upon reasonable request.

Appendix A: Wedge size convergence

In this appendix, we verify the convergence of the numerical experiments with respect to the wedge size. We repeat the numerical experiments with the 1/3 wedge torus model, and compare plasma profiles and turbulent frequency spectra. In Fig.25, we compare radial profiles of the density, the parallel flow, and the temperature obtained from the numerical experiments with the 1/3 and 1/6 wedge torus models, which show negligible difference between these models. This indicates the corresponding particle, momentum, and energy transport transport is also converged between the 1/3 and 1/6 wedge torus models. Figure 26 shows the frequency spectra of the electrostatic potential measured in the numerical experiments with the 1/3 wedge torus model. Here, the definitions of plots are the same as those in Fig.23. Figures 26(a) and 26(c) respectively show the QCMs in the LOC phase and the broad-band spectrum in the SOC phase as in Fig.23. However, the structures of QCMs are slightly different from the 1/6 wedge torus model. In the 1/6 wedge torus model, the primary and secondary peaks are formed by adjacent toroidal modes, $n = 12$ and $n = 18$. In the 1/3 wedge torus model, the toroidal mode numbers of the primary and secondary peaks are unchanged, while there exists a subdominant mode with $n = 15$ in between them. Therefore, in addition to the enhancement of the frequency gap between adjacent toroidal modes due to the Doppler shift, some nonlinear coupling mechanism to selectively excite $n = 12$ and $n = 18$ modes exists. This issue will be addressed in future works.

Appendix B: Parallel flows of bulk and impurity ions

In this appendix, we verify the difference of parallel flows of bulk and impurity ions based on the neoclassical parallel momentum balance equations. In the neoclassical benchmark, we consider multi-species plasmas with kinetic electrons, D ions, and C impurity ions in a circular concentric tokamak configuration with $R_0/a = 5$, $a/\rho_{tD} = 150$, and $q(r) = 0.85 + 2.18(r/a)^2$, $m_D/m_e = 3,672$, and $Z_{eff} = 4$. The initial density and temperature profiles are given as

$$n_s(r) = n_{0s} \exp\left[-\frac{\Delta_{ns}}{L_{ns}} \tanh\left(\frac{r-r_0}{\Delta_{ns}}\right)\right], \tag{B1}$$

$$T_s(r) = T_{0s} \exp\left[-\frac{\Delta_{ts}}{L_{ts}} \tanh\left(\frac{r-r_0}{\Delta_{ts}}\right)\right], \tag{B2}$$

where $R_0/L_{ns} = R_0/L_{ts} = 2.22$, $\Delta_{ns} = \Delta_{ts} = 0.3a$, and $r_0 = 0.5a$. The normalized collisionality $\nu^*_{s,s'} \equiv qR/(\varepsilon^{3/2} v_{ts} \tau_{s,s'})$ at the mid-radius is given as $\nu^*_{e,D} = 0.08, \nu^*_{D,D} = 0.08$, and $\nu^*_{C,D} = 2.49$, where $\tau_{s,s'}$ is the collision time. The benchmark

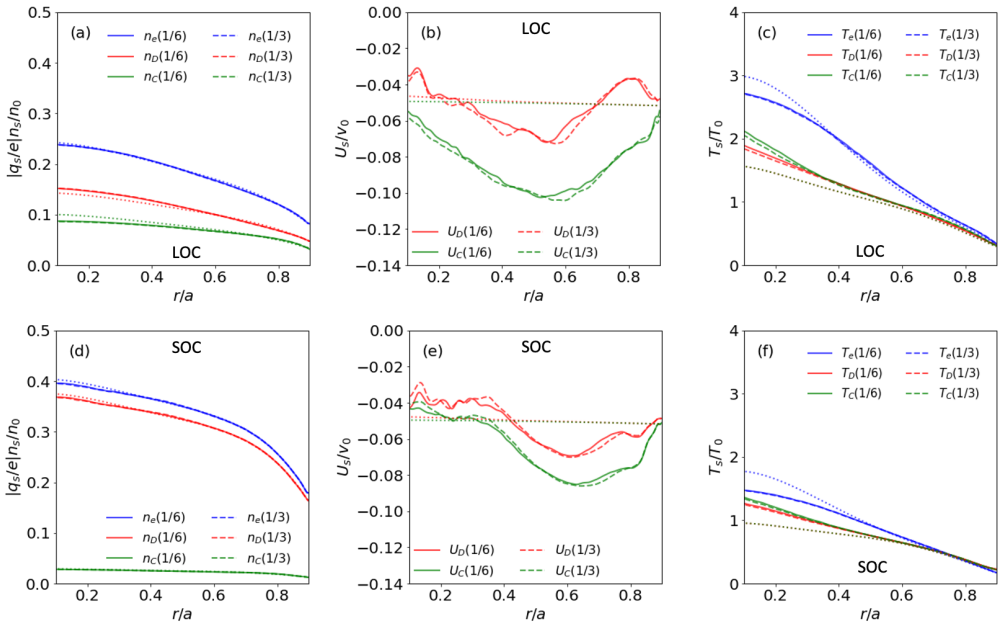

FIG. 25. Radial profiles of (a),(d) the density, (b),(e) the parallel flow, and (c),(f) the temperature averaged over $tv_0/R = 900 \sim 1000$. (a)-(c) and (d)-(f) respectively show the numerical experiments in the LOC and SOC phases. Solid and dashed curves respectively show the results with the 1/6 and 1/3 wedge torus models, and dotted curves show the initial profiles.

calculation is performed in the axisymmetric limit on 4D grids $(N_R, N_\zeta, N_Z, N_{v_\parallel}, N_{v_\perp}) = (160, 1, 160, 96, 24)$.

Figure 27 shows a comparison of parallel currents between GT5D and the neoclassical theory[67,68]. Here, the neoclassical results are computed using the Matrix Inversion code[68], which computes the parallel components of the momentum and heat flow balance equations

$$[\mathbf{M} - \mathbf{L}]\vec{X} = \mathbf{M}\vec{V}. \tag{B3}$$

Here, $\mathbf{L}$ and $\mathbf{M}$ are matrices given by the parallel friction coefficients and the viscosity coefficients, respectively. The parallel components of flow and heat flux $\vec{X}$ and the thermodynamic force $\vec{V}$ are respectively given as

$$\vec{X} = \begin{bmatrix} \langle \mathbf{B}\cdot\mathbf{U}_e\rangle \\ \langle \mathbf{B}\cdot\mathbf{U}_D\rangle \\ \langle \mathbf{B}\cdot\mathbf{U}_C\rangle \\ 2\langle \mathbf{B}\cdot\mathbf{q}_e\rangle/(5p_e) \\ 2\langle \mathbf{B}\cdot\mathbf{q}_D\rangle/(5p_D) \\ 2\langle \mathbf{B}\cdot\mathbf{q}_C\rangle/(5p_C) \end{bmatrix}, \quad \vec{V} = \begin{bmatrix} V_{1e} \\ V_{1D} \\ V_{1C} \\ V_{2e} \\ V_{2D} \\ V_{2C} \end{bmatrix}, \tag{B4}$$

where the thermodynamic force is given as

$$V_{1s} = -\frac{F}{B\nabla\psi}\left[\frac{d\phi}{dr} + \frac{1}{q_s n_s}\frac{dp_s}{dr}\right], \tag{B5}$$

$$V_{2s} = -\frac{F}{B\nabla\psi}\frac{dT_s}{dr}. \tag{B6}$$

By inverting Eq.(B3) as

$$\vec{X} = A\vec{V}, \tag{B7}$$

and substituting ϕ, n_s, and T_s from GT5D, one can estimate parallel flows for each species, where $A = [\mathbf{L} - \mathbf{M}]^{-1}\cdot\mathbf{M}$. Also, the bootstrap current is estimated as $\langle \mathbf{B}\cdot\mathbf{J}\rangle = \sum_s q_s n_s \langle \mathbf{B}\cdot\mathbf{U}_s\rangle$. The benchmark result shows good quantitative agreements, indicating that GT5D can correctly compute the difference of ion parallel flows in multi-species plasmas. In the current benchmark case involving a high fraction of C impurity ions, the C rotation develops in the counter-current direction with respect to D rotation.

[1] ITER Physics Expert Groups on Confinement and Transport and Confinement Modelling and Database, I. P. B. Editors, and I. EDA, "Chapter 2: Plasma confinement and transport," Nucl. Fusion **39**, 2175–2249 (1999).
[2] J. Rice, J. Citrin, N. Cao, P. Diamond, M. Greenwald, and B. Grierson, "Understanding LOC/SOC phenomenology in tokamaks," Nucl. Fusion **60**, 105001 (2020).
[3] X. Garbet, J. Payan, C. Laviron, P. Devynck, S. K. Saha, H. Capes, X. P. Chen, J. P. Coulon, C. Gil, and G. R. Harris, "Turbulence and energy confinement in TORE SUPRA Ohmic discharges," Nuclear fusion **32**, 2147 (1992).
[4] J. E. Rice, C. Gao, M. L. Reinke, P. H. Diamond, N. T. Howard, H. J. Sun, I. Cziegler, A. E. Hubbard, Y. A. Podpaly, and W. L. Rowan, "Non-local heat transport, rotation reversals and up/down impurity density asymmetries in Alcator C-Mod ohmic L-mode plasmas," Nuclear Fusion **53**, 033004 (2013).
[5] A. Krämer-Flecken, V. Dreval, S. Soldatov, A. Rogister, and V. Vershkov, "Turbulence studies with means of reflectometry at TEXTOR," Nuclear fusion **44**, 1143 (2004).
[6] H. Arnichand, R. Sabot, S. Hacquin, A. Krämer-Flecken, X. Garbet, J. Citrin, C. Bourdelle, G. Hornung, J. Bernardo, C. Bottereau, F. Clairet, G. Falchetto, and J. Giacalone, "Quasi-coherent modes and electron-driven turbulence," Nucl. Fusion **54**, 123017 (2014).
[7] H. Arnichand, R. Sabot, S. Hacquin, A. Krämer-Flecken, C. Bourdelle, J. Citrin, X. Garbet, J. C. Giacalone, R. Guirlet, and J. C. Hillesheim, "Dis-

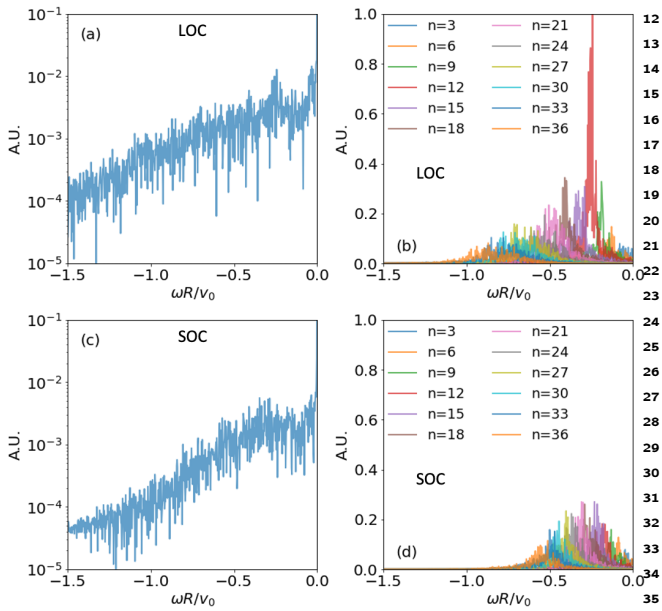

FIG. 26. Frequency spectra of the electrostatic potential in the numerical experiments with the 1/3 wedge torus model. The definitions of plots are the same as those in Fig.23.

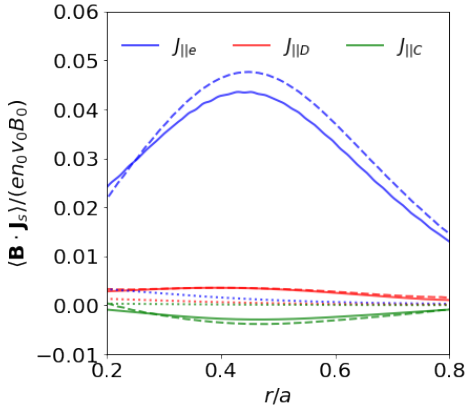

FIG. 27. Radial profiles of the parallel current of electrons, deuterium ions, and carbon impurity ions. Broken lines show the initial condition given by non-shifted Maxwellian distributions. Solid and dashed lines respectively show the results from GT5D and neoclassical theory (the matrix inversion code) at $tv_{tD}/R_0 = 250$.

criminating the trapped electron modes contribution in density fluctuation spectra," Nuclear fusion **55**, 093021 (2015).
[8]F. Romanelli, W. M. Tang, and R. B. White, "Anomalous thermal confinement in ohmically heated tokamaks," Nuclear fusion **26**, 1515 (1986).
[9]C. L. Rettig, T. L. Rhodes, J. N. Leboeuf, W. A. Peebles, E. J. Doyle, G. M. Staebler, K. H. Burrell, and R. A. Moyer, "Search for the ion temperature gradient mode in a tokamak plasma and comparison with theoretical predictions," Physics of Plasmas **8**, 2232–2237 (2001).
[10]J. E. Rice, M. J. Greenwald, Y. A. Podpaly, M. L. Reinke, P. H. Diamond, J. W. Hughes, N. T. Howard, Y. Ma, I. Cziegler, B. P. Duval, P. C. Ennever, D. Ernst, C. L. Fiore, C. Gao, J. H. Irby, E. S. Marmar, M. Porkolab, N. Tsujii, and S. M. Wolfe, "Ohmic energy confinement saturation and core toroidal rotation reversal in Alcator C-Mod plasmas," Physics of Plasmas **19**, 056106 (2012).
[11]C. Sung, A. White, N. Howard, C. Oi, J. Rice, C. Gao, P. Ennever, M. Porkolab, F. Parra, D. Mikkelsen, D. Ernst, J. Walk, J. Hughes, J. Irby, C. Kasten, A. Hubbard, M. Greenwald, and the Alcator C-Mod Team, "Changes in core electron temperature fluctuations across the ohmic energy confinement transition in Alcator C-Mod plasmas," Nucl. Fusion **53**, 083010 (2013).
[12]R. McDermott, C. Angioni, G. Conway, R. Dux, E. Fable, R. Fischer, T. Pütterich, F. Ryter, E. Viezzer, and the ASDEX Upgrade Team, "Core intrinsic rotation behaviour in ASDEX Upgrade ohmic L-mode plasmas," Nucl. Fusion **54**, 043009 (2014).
[13]C. Gao, J. Rice, H. Sun, M. Reinke, N. Howard, D. Mikkelson, A. Hubbard, M. Chilenski, J. Walk, J. Hughes, P. Ennever, M. Porkolab, A. White, C. Sung, L. Delgado-Aparicio, S. Baek, W. Rowan, M. Brookman, M. Greenwald, R. Granetz, S. Wolfe, E. Marmar, and The Alcator C-Mod Team, "Non-local heat transport in Alcator C-Mod ohmic L-mode plasmas," Nucl. Fusion **54**, 083025 (2014).
[14]J. Bernardo, C. Fenzi, C. Bourdelle, Y. Camenen, H. Arnichand, J. P. S. Bizarro, S. Cortes, X. Garbet, Z. O. Guimarães-Filho, T. Aniel, J.-F. Artaud, F. Clairet, P. Cottier, J. Gunn, P. Lotte, and the Tore Supra Team, "Density impact on toroidal rotation in Tore Supra: Experimental observations and theoretical investigation," Plasma Phys. Control. Fusion **57**, 035002 (2015).
[15]Y. Shi, J. Kwon, P. Diamond, W. Ko, M. Choi, S. Ko, S. Hahn, D. Na, J. Leem, J. Lee, S. Yang, K. Lee, M. Joung, J. Jeong, J. Yoo, W. Lee, J. Lee, Y. Bae, S. Lee, S. Yoon, K. Ida, and Y.-S. Na, "Intrinsic rotation reversal, non-local transport, and turbulence transition in KSTAR L-mode plasmas," Nucl. Fusion **57**, 066040 (2017).
[16]D. Na, Y.-S. Na, C. Angioni, S. Yang, J. Kwon, H. Jhang, Y. Camenen, S. Lee, Y. Shi, W. Ko, J. Lee, T. Hahm, and KSTAR Team, "A comprehensive study on rotation reversal in KSTAR: Experimental observations and modelling," Nucl. Fusion **57**, 126008 (2017).
[17]J. A. Lee, W. Lee, J. M. Kwon, S. H. Ko, J. Leem, G. S. Yun, H. K. Park, Y. S. Park, K. W. Kim, and N. C. Luhmann Jr, "Observation of electron driven quasi-coherent modes and their connection with core intrinsic rotation in KSTAR ECH and ohmic L-mode plasmas," Physics of Plasmas **25**, 022513 (2018).
[18]N. Cao, J. Rice, P. Diamond, A. White, S. Baek, M. Chilenski, J. Hughes, J. Irby, M. Reinke, P. Rodriguez-Fernandez, and the Alcator C-Mod Team, "Hysteresis as a probe of turbulent bifurcation in intrinsic rotation reversals on Alcator C-Mod," Nucl. Fusion **59**, 104001 (2019).
[19]L. Lin, M. Porkolab, E. M. Edlund, J. C. Rost, M. Greenwald, N. Tsujii, J. Candy, R. E. Waltz, and D. R. Mikkelsen, "Studies of turbulence and transport in Alcator C-Mod ohmic plasmas with phase contrast imaging and comparisons with gyrokinetic simulations," Plasma Phys. Control. Fusion **51**, 065006 (2009).
[20]C. Angioni, R. M. McDermott, F. J. Casson, E. Fable, A. Bottino, R. Dux, R. Fischer, Y. Podoba, T. Pütterich, F. Ryter, and E. Viezzer, "Intrinsic Toroidal Rotation, Density Peaking, and Turbulence Regimes in the Core of Tokamak Plasmas," Phys. Rev. Lett. **107**, 215003 (2011).
[21]M. Porkolab, J. Dorris, P. Ennever, C. Fiore, M. Greenwald, A. Hubbard, Y. Ma, E. Marmar, Y. Podpaly, M. L. Reinke, J. E. Rice, J. C. Rost, N. Tsujii, D. Ernst, J. Candy, G. M. Staebler, and R. E. Waltz, "Transport and turbulence studies in the linear ohmic confinement regime in Alcator C-Mod," Plasma Phys. Control. Fusion **54**, 124029 (2012).
[22]P. Ennever, M. Porkolab, J. Candy, G. Staebler, M. L. Reinke, J. E. Rice, J. C. Rost, D. Ernst, C. Fiore, J. Hughes, J. Terry, and Alcator C-Mod Team, "The effects of dilution on turbulence and transport in C-Mod ohmic plasmas and comparisons with gyrokinetic simulations," Phys. Plasmas **22**, 072507 (2015).
[23]J. Citrin, H. Arnichand, J. Bernardo, C. Bourdelle, X. Garbet, F. Jenko, S. Hacquin, M. J. Pueschel, and R. Sabot, "Comparison between measured and predicted turbulence frequency spectra in ITG and TEM regimes," Plasma Phys. Control. Fusion **59**, 064010 (2017).
[24]W. X. Wang, B. A. Grierson, S. Ethier, J. Chen, E. Startsev, and P. H. Diamond, "Understanding and predicting profile structure and parametric scaling of intrinsic rotation," Physics of Plasmas **24**, 092501 (2017).

[25] B. A. Grierson, W. X. Wang, S. Ethier, G. M. Staebler, D. J. Battaglia, J. A. Boedo, J. S. DeGrassie, and W. M. Solomon, "Main-ion intrinsic toroidal rotation profile driven by residual stress torque from ion temperature gradient turbulence in the DIII-D tokamak," Physical Review Letters **118**, 015002 (2017).

[26] B. A. Grierson, C. Chrystal, S. R. Haskey, W. X. Wang, T. L. Rhodes, G. R. McKee, K. Barada, X. Yuan, M. F. F. Nave, A. Ashourvan, and C. Holland, "Main-ion intrinsic toroidal rotation across the ITG/TEM boundary in DIII-D discharges during ohmic and electron cyclotron heating," Physics of Plasmas **26**, 042304 (2019).

[27] I. Erofeev, E. Fable, C. Angioni, R. McDermott, and The ASDEX Upgrade Team, "Theory-based modeling of LOC–SOC transitions in ASDEX Upgrade," Nucl. Fusion **57**, 126067 (2017).

[28] H. Arnichand, J. Citrin, S. Hacquin, R. Sabot, A. Krämer-Flecken, X. Garbet, C. Bourdelle, C. Bottereau, F. Clairet, J. C. Giacalone, Z. O. Guimarães-Filho, R. Guirlet, G. Hornung, A. Lebschy, P. Lotte, P. Maget, A. Medvedeva, D. Molina, V. Nikolaeva, D. Prisiazhniuk, the Tore Supra, and the ASDEX Upgrade teams, "Identification of trapped electron modes in frequency fluctuation spectra," Plasma Phys. Control. Fusion **58**, 014037 (2016).

[29] W. Hornsby, C. Angioni, Z. Lu, E. Fable, I. Erofeev, R. McDermott, A. Medvedeva, A. Lebschy, A. Peeters, and The ASDEX Upgrade Team, "Global gyrokinetic simulations of intrinsic rotation in ASDEX Upgrade Ohmic L-mode plasmas," Nucl. Fusion **58**, 056008 (2018).

[30] B. Scott and J. Smirnov, "Energetic consistency and momentum conservation in the gyrokinetic description of tokamak plasmas," Physics of Plasmas **17**, 112302 (2010).

[31] J. Abiteboul, X. Garbet, V. Grandgirard, S. J. Allfrey, P. Ghendrih, G. Latu, Y. Sarazin, and A. Strugarek, "Conservation equations and calculation of mean flows in gyrokinetics," Physics of Plasmas **18**, 082503 (2011).

[32] Y. Idomura, "Accuracy of momentum transport calculations in full- f gyrokinetic simulations," Comput. Sci. Disc. **5**, 014018 (2012).

[33] M. Nakata and Y. Idomura, "Plasma size and collisionality scaling of ion-temperature-gradient-driven turbulence," Nucl. Fusion **53**, 113039 (2013).

[34] G. Dif-Pradalier, G. Hornung, X. Garbet, P. Ghendrih, V. Grandgirard, G. Latu, and Y. Sarazin, "The E × B staircase of magnetised plasmas," Nucl. Fusion **57**, 066026 (2017).

[35] Y. Idomura, M. Ida, T. Kano, N. Aiba, and S. Tokuda, "Conservative global gyrokinetic toroidal full-f five-dimensional Vlasov simulation," Computer Physics Communications **179**, 391–403 (2008).

[36] Y. Idomura, H. Urano, N. Aiba, and S. Tokuda, "Study of ion turbulent transport and profile formations using global gyrokinetic full- f Vlasov simulation," Nucl. Fusion **49**, 065029 (2009).

[37] Y. Idomura, "A new hybrid kinetic electron model for full-f gyrokinetic simulations," Journal of Computational Physics **313**, 511–531 (2016).

[38] Y. Idomura, K. Obrejan, Y. Asahi, and M. Honda, "Dynamics of enhanced neoclassical particle transport of tracer impurity ions in ion temperature gradient driven turbulence," Physics of Plasmas **28**, 012501 (2021).

[39] W. W. Lee, "Gyrokinetic particle simulation model," Journal of Computational Physics **72**, 243–269 (1987).

[40] C. J. McDevitt, P. H. Diamond, Ö. D. Gürcan, and T. S. Hahm, "Toroidal Rotation Driven by the Polarization Drift," Phys. Rev. Lett. **103**, 205003 (2009).

[41] Y. Camenen, Y. Idomura, S. Jolliet, and A. Peeters, "Consequences of profile shearing on toroidal momentum transport," Nucl. Fusion **51**, 073039 (2011).

[42] Y. Asahi, V. Grandgirard, Y. Idomura, X. Garbet, G. Latu, Y. Sarazin, G. Dif-Pradalier, P. Donnel, and C. Ehrlacher, "Benchmarking of flux-driven full-F gyrokinetic simulations," Phys. Plasmas **24**, 102515 (2017).

[43] S. Satake, Y. Idomura, H. Sugama, and T.-H. Watanabe, "Benchmark tests of drift-kinetic and gyrokinetic codes through neoclassical transport simulations," Computer Physics Communications **181**, 1069–1076 (2010).

[44] S. Matsuoka, Y. Idomura, and S. Satake, "Neoclassical transport benchmark of global full-f gyrokinetic simulation in stellarator configurations," Phys. Plasmas **25**, 022510 (2018).

[45] Y. Idomura, "Full- f gyrokinetic simulation over a confinement time," Physics of Plasmas **21**, 022517 (2014).

[46] S. Jolliet and Y. Idomura, "Plasma size scaling of avalanche-like heat transport in tokamaks," Nucl. Fusion **52**, 023026 (2012).

[47] Y. Idomura, T. Ina, Y. Ali, and T. Imamura, "Acceleration of Fusion Plasma Turbulence Simulations using the Mixed-Precision Communication-Avoiding Krylov Method," in *SC20: International Conference for High Performance Computing, Networking, Storage and Analysis* (IEEE, Atlanta, GA, USA, 2020) pp. 1–13.

[48] M. Sato, Y. Ishikawa, H. Tomita, Y. Kodama, T. Odajima, M. Tsuji, H. Yashiro, M. Aoki, N. Shida, I. Miyoshi, K. Hirai, A. Furuya, A. Asato, K. Morita, and T. Shimizu, "Co-Design for A64FX Manycore Processor and "Fugaku"," in *SC20: International Conference for High Performance Computing, Networking, Storage and Analysis* (IEEE, Atlanta, GA, USA, 2020) pp. 1–15.

[49] Y. Sarazin, J. Hillairet, J.-L. Duchateau, K. Gaudimont, R. Varennes, X. Garbet, P. Ghendrih, R. Guirlet, B. Pégourié, and A. Torre, "Impact of scaling laws on tokamak reactor dimensioning," Nucl. Fusion **60**, 016010 (2020).

[50] Y. Idomura and M. Nakata, "Plasma size and power scaling of ion temperature gradient driven turbulence," Physics of Plasmas **21**, 020706 (2014).

[51] Y. Idomura, "Isotope and plasma size scaling in ion temperature gradient driven turbulence," Physics of Plasmas **26**, 120703 (2019).

[52] J. W. Connor, J. B. Taylor, and H. R. Wilson, "Shear damping of drift waves in toroidal plasmas," Physical review letters **70**, 1803 (1993).

[53] J. Y. Kim and M. Wakatani, "Radial structure of high-mode-number toroidal modes in general equilibrium profiles," Physical review letters **73**, 2200 (1994).

[54] R. E. Waltz, G. M. Staebler, and W. M. Solomon, "Gyrokinetic simulation of momentum transport with residual stress from diamagnetic level velocity shears," Physics of Plasmas **18**, 042504 (2011).

[55] R. Buchholz, Y. Camenen, F. J. Casson, S. R. Grosshauser, W. A. Hornsby, P. Migliano, and A. G. Peeters, "Toroidal momentum transport in a tokamak due to profile shearing," Physics of Plasmas **21**, 062304 (2014).

[56] M. Mattioli, R. Giannella, R. Myrnas, C. Demichelis, B. Denne-Hinnov, T. D. De Wit, and G. Magyar, "Laser blow-off injected impurity particle confinement times in JET and Tore Supra," Nuclear Fusion **35**, 1115 (1995).

[57] A. Peeters, C. Angioni, A. Bortolon, Y. Camenen, F. Casson, B. Duval, L. Fiederspiel, W. Hornsby, Y. Idomura, T. Hein, N. Kluy, P. Mantica, F. Parra, A. Snodin, G. Szepesi, D. Strintzi, T. Tala, G. Tardini, P. de Vries, and J. Weiland, "Overview of toroidal momentum transport," Nucl. Fusion **51**, 094027 (2011).

[58] P. Diamond, Y. Kosuga, Ö. Gürcan, C. McDevitt, T. Hahm, N. Fedorczak, J. Rice, W. Wang, S. Ku, J. Kwon, G. Dif-Pradalier, J. Abiteboul, L. Wang, W. Ko, Y. Shi, K. Ida, W. Solomon, H. Jhang, S. Kim, S. Yi, S. Ko, Y. Sarazin, R. Singh, and C. Chang, "An overview of intrinsic torque and momentum transport bifurcations in toroidal plasmas," Nucl. Fusion **53**, 104019 (2013).

[59] Y. Camenen, A. G. Peeters, C. Angioni, F. J. Casson, W. A. Hornsby, A. P. Snodin, and D. Strintzi, "Transport of Parallel Momentum Induced by Current-Symmetry Breaking in Toroidal Plasmas," Phys. Rev. Lett. **102**, 125001 (2009).

[60] R. R. Dominguez and G. M. Staebler, "Anomalous momentum transport from drift wave turbulence," Physics of Fluids B: Plasma Physics **5**, 3876–3886 (1993).

[61] Ö. Gürcan, P. H. Diamond, and T. S. Hahm, "Spatial and spectral evolution of turbulence," Physics of plasmas **14**, 055902 (2007).

[62] Ö. D. Gürcan, P. H. Diamond, P. Hennequin, C. J. McDevitt, X. Garbet, and C. Bourdelle, "Residual parallel Reynolds stress due to turbulence intensity gradient in tokamak plasmas," Physics of Plasmas **17**, 112309 (2010).

[63] J. Y. Kim, Y. Kishimoto, M. Wakatani, and T. Tajima, "Poloidal shear flow effect on toroidal ion temperature gradient mode: A theory and simulation," Physics of Plasmas **3**, 3689–3695 (1996).

[64] Y. Kishimoto, J.-Y. Kim, W. Horton, T. Tajima, M. J. LeBrun, and H. Shirai, "Toroidal mode structure in weak and reversed magnetic shear plasmas and its role in the internal transport barrier," Plasma Phys. Control. Fusion **41**, A663–A678 (1999).

[65] R. E. Waltz, R. L. Dewar, and X. Garbet, "Theory and simulation of rotational shear stabilization of turbulence," Physics of Plasmas **5**, 1784–1792 (1998).

[66] X. Garbet, N. Dubuit, E. Asp, Y. Sarazin, C. Bourdelle, P. Ghendrih, and G. T. Hoang, "Turbulent fluxes and entropy production rate," Physics of Plasmas **12**, 082511 (2005).

[67] S. Hirshman and D. Sigmar, "Neoclassical transport of impurities in tokamak plasmas," Nucl. Fusion **21**, 1079–1201 (1981).

[68] M. Kikuchi, M. Azumi, S. Tsuji, K. Tani, and H. Kubo, "Bootstrap current during perpendicular neutral injection in JT-60," Nucl. Fusion **30**, 343–355 (1990).

[69] R. Varennes, X. Garbet, L. Vermare, Y. Sarazin, G. Dif-Pradalier, V. Grandgirard, P. Ghendrih, P. Donnel, M. Peret, K. Obrejan, and E. Bourne, "Synergy of Turbulent Momentum Drive and Magnetic Braking," Phys. Rev. Lett. **128**, 255002 (2022).

[70] C. Fenzi, X. Garbet, E. Trier, P. Hennequin, C. Bourdelle, T. Aniel, G. Colledani, P. Devynck, C. Gil, and Ö. Gürcan, "On plasma rotation with toroidal magnetic field ripple and no external momentum input," Nuclear Fusion **51**, 103038 (2011).